Global and Planetary Change 259 (2026) 105366

Contents lists available at ScienceDirect

Global and Planetary Change

journal homepage: www.elsevier.com/locate/gloplacha

Research Article

Evolution of the primary productivity recovery at the Cretaceous-Paleogene boundary at the Caravaca distal section (Spain)☆

Claudia Sosa-Montes de Oca [a,b,*], Marta Rodrigo-Gámiz [b], Gines A. de Gea [c], Cristina Sequero [d], Yiming Zhang [a], Panteleimon Prokopiou [a], José Manuel Castro [c], Mª. Luisa Quijano [e], Richard D. Pancost [a]

[a] Organic Geochemistry Unit, The Cabot Institute for the Environment, School of Earth Sciences, School of Chemistry, University of Bristol, BS8 1TS, UK
[b] Departamento de Estratigrafía y Paleontología, Universidad de Granada, Avda. Fuentenueva s/n, 18002 Granada, Spain
[c] Departamento de Geología and CEACTEMA, Universidad de Jaén, Campus Las Lagunillas, 23071 Jaén, Spain
[d] Departamento de Geodinámica, Estratigrafía y Paleontología, Universidad Complutense de Madrid, C/ de José Antonio Novais 12, Moncloa-Aravaca, 28040 Madrid, Spain
[e] Departamento de Química Inorgánica y Orgánica and CEACTEMA, Universidad de Jaén, Campus Las Lagunillas, 23071 Jaén, Spain

ARTICLE INFO

Editor: Dr. Maoyan Zhu

Keywords:
Cretaceous/Paleogene boundary
Organic matter source
Detrital input
Stable isotopes
Phytoplankton and bacterial communities
High-resolution paleoenvironmental reconstruction
Distal section

ABSTRACT

The Cretaceous-Paleogene boundary represents the latest of the five major mass extinctions in Earth's history. Previous biomarker studies at distal K-Pg sites have suggested transient changes; however, the lack of high-resolution and extended records limits our understanding of the mechanisms and duration of post-impact biotic recovery.

We performed a multiproxy analysis at continuous cm-scale resolution across an ~300 cm-thick K-Pg boundary interval at the Caravaca distal section (SE Spain) that spans ~22 kyr before to ~220 kyr after the K-Pg event. We analysed the section's biostratigraphy and explored changes in organic matter composition (*n*-alkanes, acyclic isoprenoids, steranes and hopanes), trace elemental ratios and concentrations (K/Al, Ti/Al, Ba/Ti, Ca/Al, Ir and $CaCO_3$), and isotopic compositions of both bulk ($\delta^{13}C_{carb}$, $\delta^{13}C_{org}$) and high-molecular-weight *n*-alkanes ($\delta^{13}C_{HMW}$). Changes in the organic matter abundance and provenance, isotopic composition and in trace element distributions were observed, mainly in the post-impact ejecta layer and boundary clay layer (representing ca. ~10 kyr after impact). Although many biomarker mass accumulation rates exhibit a decrease and slow recovery after the K-Pg, an increase in some putative marine productivity biomarkers (pristane and phytane; LMW *n*-alkanes) is recorded from 5 kyrs before to 30 kyrs after the K-Pg mass extinction. Intriguingly, a co-eval variation in some inorganic terrestrial/extraterrestrial input (Ti/Al, K/Al, Ir) and some biomarker proxies with an anomalous excursion in the organic carbon isotope record ($\delta^{13}C_{org}$) suggest transient change in organic matter, perhaps reflecting an erosive event associated with the impact. This erosive event appears to be related to the remobilization of less thermally or diagenetically altered terrestrial organic matter, making it analogous to but distinct from studied distal Cretaceous-Paleogene sections such as Agost, in Spain, and Mid-Waipara, in New Zealand which were characterised by remobilization of thermally mature organic matter. Thus, with our novel high-resolution primary productivity evolution results, we can evidence for first time, heterogeneity on biomarker's responses in distal the Cretaceous-Paleogene boundary sites.

1. Introduction

The Cretaceous-Paleogene (K-Pg) boundary, dated ~66.0 Myr (Sprain et al., 2018), is associated with the most recent mass extinction event and the disappearance of about 72% of marine and continental species (D'Hondt, 2005). This mass extinction is typically attributed to the catastrophic environmental consequences of the Chicxulub Impact (Alvarez et al., 1980; Smit and Hertogen, 1980; Schulte et al., 2010;

☆ This article is part of a Special issue entitled: 'Oceanic Anoxic Event' published in Global and Planetary Change.

* Corresponding author at: Organic Geochemistry Unit, The Cabot Institute for the Environment, School of Earth Sciences, School of Chemistry, University of Bristol, BS8 1TS, UK.
E-mail address: claudia.sosamontesdeoca@bristol.ac.uk (C. Sosa-Montes de Oca).

https://doi.org/10.1016/j.gloplacha.2026.105366
Received 4 June 2025; Received in revised form 20 January 2026; Accepted 6 February 2026
Available online 14 February 2026

Pälike, 2013; Hull et al., 2020; Morgan et al., 2022). However, other mechanisms, such as the volcanism associated with the Deccan Traps, have also been invoked as contributing to theses environmental changes (Li et al., 2022; Schoene et al., 2015, 2019).

Much work has focused on understanding the short- to long-term effects of the Chicxulub impact on the global environmental system, including the time frame required for the re-establishment of pre-impact environmental conditions and the microbial and non-fossilizing phytoplankton communities. The many K-Pg sections worldwide exhibit different features depending on the distance to the impact in the Gulf of Mexico (Chicxulub structure) (Hildebrand et al., 1991; Swisher Ill et al., 1990), e.g.: i) very proximal, less than 500 km from impact site: ii) proximal, between 500 and 1000 km from impact site; iii) intermediate, between 1000 and 5000 km from Chicxulub impact site; and iv) distal, more than 5000 kms from impact site. Although proximal K-Pg marine deposits provide information about the immediate physical effects of the impact and associated environmental changes (Bralower et al., 2020a; Lowery and Bralower, 2022; Morgan et al., 2022; Schaefer et al., 2020), the distal sections are particularly important for assessing the global consequences of the K-Pg boundary and the nature of both environmental and biotic recovery after this impact event (Bralower et al., 2020; Henehan et al., 2019; Sepúlveda et al., 2019).

In previous molecular fossil (i.e. biomarker) based studies focused on several distal K-Pg sites (> 5000 km from Chicxulub impact site), such as the Stevns Klint (Denmark), Mid-Waipara (New Zealand) and Agost (Spain) sections (Bralower et al., 2020; Sepúlveda et al., 2009; Sosa-Montes de Oca et al., 2023; Sosa-Montes de Oca et al., 2021), only minor changes in the non-fossilizing phytoplankton community across the boundary were observed, in particular, a transient change in marine algal (sterane and *n*-alkane) biomarker distributions within 10 kyrs after impact. However, in proximal K-Pg sites, large and persistent changes have been observed in both the organic matter (OM) abundance and biomarker assemblages across the boundary (Schaefer et al., 2020; Sosa-Montes de Oca et al., 2024). Distal sites do record other environmental changes, albeit often associated with a rapid return to pre-impact conditions. The Caravaca and Agost marine K-Pg distal sections, located in southeastern Spain, and the El Kef section, located in Tunisia, represent some of the most continuous, well-preserved and well-studied K-Pg boundary distal sections worldwide (e.g. Molina et al., 2005; Rodríguez-Tovar et al., 2006). Inorganic geochemistry and ichnological analyses on the Spanish sections (Sosa-Montes de Oca et al., 2020; Sosa-Montes de Oca et al., 2013, 2016, 2018a, 2018b) revealed decreased bottom water oxygenation associated with the ejecta layer, but the recovery to previous oxic conditions occurred almost instantaneously, allowing the macrobenthic community to quickly recolonize the substrate (Laska et al., 2017; Rodríguez-Tovar, 2005, 2024; Rodríguez-Tovar et al., 2006; Rodríguez-Tovar and Uchman, 2004; Rodríguez-Tovar and Uchman, 2006; Rodríguez-Tovar and Uchman, 2004; Sosa-Montes de Oca et al., 2020).

A limitation of those previous studies – and a potential reason for the lack of biomarker change at the marine distal sites – is their limited stratigraphic resolution and range, with previous studies often focusing on sections only a few tens of cm in total thickness. For example, previous biomarkers analyses at the Caravaca section revealed a spike of pyrosynthetic polycyclic aromatic hydrocarbons related to an abrupt decrease in organic $\delta^{13}C$ (Arinobu et al., 1999) and the influx of terrestrial biomarkers into the marine environment after K-Pg boundary (Arinobu et al., 2005; Mizukami et al., 2013). However, these (and other) studies covered only a short-time interval before and after K-Pg boundary, only span between 7 kyrs before to 30 kyrs after K-Pg boundary. Therefore, long-term K-Pg records, like we got at the Caravaca section, are e ssential for contextualizing these inferred changes in OM sources (terrestrial, marine or reworked) by providing a baseline of pre- and post-K-Pg variability. Terrestrial (e.g., land plants) and marine (e.g., algal, bacterial and archaeal) OM biomarkers can be used to infer changes in aeolian, fluvial and erosive inputs of the former and productivity changes in the latter (e.g., Cranwell et al., 1987; Eglinton and Hamilton, 1967; Huang and Meinschew, 1979; Rontani and Volkman, 2003). Thus, here we report extended organic geochemical record to improve our understanding of the long-term response of the pre and post-impact biotic changes/recovery. We present a multiproxy analysis across an ~300 cm-thick K-Pg boundary interval at the Caravaca marine distal section (SE Spain) that spans the ~22 kyr preceding and ~ 220 kyr following the K-Pg event (Arenillas et al., 2004; Gilabert et al., 2021). To complement interpretation of biomarker changes, we also determined stable carbon and oxygen isotope values (bulk and *n*-alkanes of inferred terrestrial origin) and major and trace element ratios (Ca/Al, K/Al, Ba/Ti, Ti/Al, Ir, $CaCO_3$). We focus on the distribution of specific phytoplankton (e.g. pristane, phytane, *n*-alkanes, steranes), higher plant (high-molecular-weight *n*-alkanes) and bacterial (hopanes) biomarkers, in order to assess changes in paleoenvironmental conditions, OM inputs, and the composition of microbial and non-fossilizing phytoplankton community assemblages both across the K-Pg event and for an extended interval preceding and following it.

2. Geological setting

The K-Pg boundary section at Caravaca (38°04′36.39N, 1°52′41.45W) is located on the NW side of road C-336, about 4 km southwest of the town of Caravaca (Murcia, Spain), in the Barranco del Gredero (Fig.1). The lithology in ascending order is comprised by the uppermost Cretaceous (upper Maastrichtian) sediments that consist of gray calcareous marlstones and marlstones (unit a), and the overlying lowermost Paleogene (lower Danian) sediments. The latter include a 2–3-mm-thick red clay layer (the ejecta layer - unit b), a 6 cm-thick blackish-gray clay layer (the boundary clay - unit c) with a gradual increase in carbonate content (related to the recovery of biological productivity; e.g., Tribovillard et al., 2006), and light marly limestones (unit d) (Fig. 2) (see for more details Sosa-Montes de Oca et al., 2013). The Caravaca distal section is thought to represent deposition at bathyal paleowater depths of ~1000 m (Schulte et al., 2010) and at around 27–30° N paleolatitude (Smith et al., 1981) at the time of the impact event.

The ejecta layer (unit b) at the Caravaca distal section marks the sharp contrast between the Maastrichtian and Danian, and contains impact evidence such as spherules (Glass and Burns, 1987; Smit, 1999; Smit and Klaver, 1981), iridium, platinum-group element and rare earth element (REE) anomalies, a sulphide-rich carbonaceous chondrite (Kyte, 1998; Martínez-Ruiz et al., 1997; Shukolyukov and Lugmair, 1998), and a significant decrease in Ca due to the mass extinction among pelagic calcifiers (Goderis et al., 2013; Schulte et al., 2010) (Figs. 2 and 3).

3. Materials and methods

3.1. Core description and sampling

The Caravaca section was drilled on July 2021 to obtain a complete and continuous record of the K-Pg interval with the four-above-mentioned units (a, b, c and d, see Fig. 2), ranging from the uppermost Maastrichtian to the lowermost Danian. It was recovered using a Rolatec RL 48 L drilling machine with rubber tracks from the Centro de Instrumentación Científica (CIC), University of Granada, Spain.

A total of 5 cores were obtained in the Caravaca section (Fig. 2), but only in 2 of them, CA4 and the CA5, was the K-Pg boundary (both the ejecta layer - unit b and the boundary clay - unit c) recovered. From these two cores, only the ~300 cm-thick bore hole of the K-Pg CA4 was selected for this study, as it contained a better record of the K-Pg. This core was described, measured, and then continuously sampled (~30 g was taken for each sample) at varying resolution (between 3, 4, 5 or 6 cm), depending on the unit interval and to the distance to the K-Pg. A total of 65 samples were taken for organic geochemical, total organic carbon (TOC), and stable carbon and oxygen isotope analyses ($\delta^{13}C_{carb}$

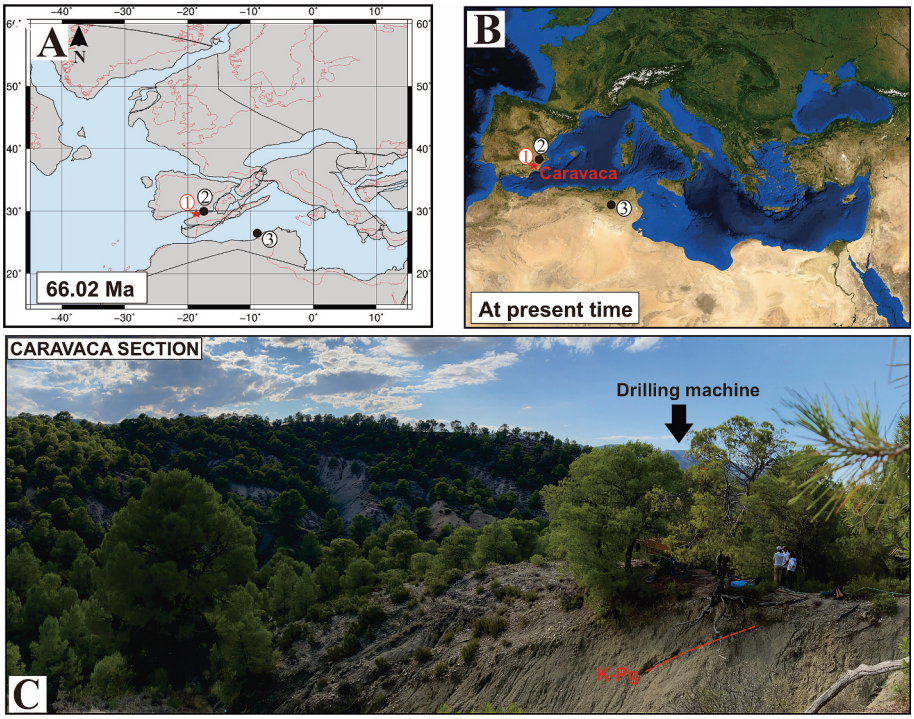

Fig. 1. Location of the K-Pg section at the Caravaca site (red colour) located in Southeast Spain. (A) 66 Ma ago. (B) at present days. Number 1 in red shows the Caravaca section, number 2 in black indicates the Agost section, number 3 in blacks shows the El Kef section. (C) Photograph of the Caravaca section taken during drilling. (For interpretation of the references to colour in this figure legend, the reader is referred to the web version of this article.)

and $\delta^{18}O$; $\delta^{13}C_{org}$). In addition, 30 samples were selected for compound specific isotope analysis (CSIA) of high-molecular-weight *n*-alkanes (>*n*-C_{29}) ($\delta^{13}C_{HMW}$). Planktonic foraminifera assemblages were examined to corroborate the continuity or the presence of hiatuses.

3.2. Micropaleontological analysis

Micropaleontological analysis of the Caravaca section is based on planktonic foraminifera, whose stratigraphic distribution is illustrated in Fig. 3 and Table 1 from supplementary material. A total of 17 samples were studied, of which 3 were below the K-Pg limit and the rest above. Sample density was greater in the first 100 cm situated above the K-Pg boundary, in order to identify the different biozones that characterize the base of the Danian. Samples were broken up with a mortar and pestle into ~1 cm chunks, soaked for at least 24 h in a solution of peroxide and borax to aid disaggregation, and then washed over a 45 μm sieve. The sieved residue was then dried overnight in an oven and analysed under a Zeiss Discovery V8 microscope for the presence/absence of bio-stratigraphically significant taxa.

The samples are rich in planktonic foraminifera, and preservation is moderate to good. For this study, the taxonomic framework used for Upper Maastrichtian is based on Robaszynski et al. (1984), Caron (1985), Nederbract (1991), Arz and Molina (2002), Arz et al. (2010) and the pforams@mikrotax website (Young et al., 2024). The planktonic foraminifera taxonomy applied to the basal Danian is based on those proposed by Luterbacher and Premoli Silva (1964), Loeblich Jr and Tappan, 1987Olsson et al. (1999), Arenillas and Arz (2000), Arenillas et al. (2004, 2007), and pforams@mikrotax website (Young et al., 2024). According to Arenillas and Arz (2000), the species *Parvularugo-blobigerina longiapertura* and *Parvularugoglobigerina eugubina* have been differentiated and used to stablish the lowermost Danian biozonation. Using the biozonation proposed by Arenillas et al. (2004) and Gilabert et al. (2021), all the biozones of the K-Pg transit were identified (Fig. 3).

3.3. XRF core-scanner analyses

High-resolution XRF core-scanning was conducted using a Itrax FixRAY located at the Centro de Instrumentación Científica (CIC) at the University of Granada (Spain). The core Caravaca CA4 presents 6 un-altered samples (MI). First, each core was cut in half; then, each half was fixed in the scanner and measured in continuous mode with a resolution that varied between 2 mm for MI5 (where the K-Pg boundary is crossed) and 4 mm resolution for the rest MI1, MI2 MI3, MI4 and MI6. A total of 58 major and trace chemical elements, between mass element 24 (Mg) and 238 (U), were measured using a 100 s count time, 30 kV X-ray voltage, and X-ray current of 2 mA. Furthermore, we used the Q-Spec program to convert point counts into concentrations (%) using Nist-610 as internal standart.

Through the K-Pg interval, large shifts in carbonate content occur, impacting most element distributions. To study elemental variability without this carbonate dilution effect, Al-normalized concentrations or recalculation on a carbonate-free basis is usually applied (Calvert and Pedersen, 1993; De Lange et al., 1987; Morford and Emerson, 1999; Tribovillard et al., 2006; Van der Weijden, 2002). We have selected the following ratios Ca/Al, Ba/Ti, K/Al, Ti/Al and Ir to locate the K-Pg boundary and to provide insights into productivity, terrigenous input and extraterrestrial contamination, complementing the biomarker results.

3.4. Organic geochemistry

3.4.1. Total organic carbon (TOC) analysis

In total, 65 samples distributed along the ~300 cm core CA4 were selected for determination of total organic carbon (TOC) contents and biomarkers. This includes 22 samples from the 100 cm-thick interval of uppermost Cretaceous sediments (unit a), 1 sample from the 0.2 cm-thick ejecta layer (unit b), 2 samples from the 6 cm-thick boundary clay (unit c), and 40 samples from the 200 cm-thick light marly limestones (unit d), with higher resolution sampling closer to the K-Pg boundary.

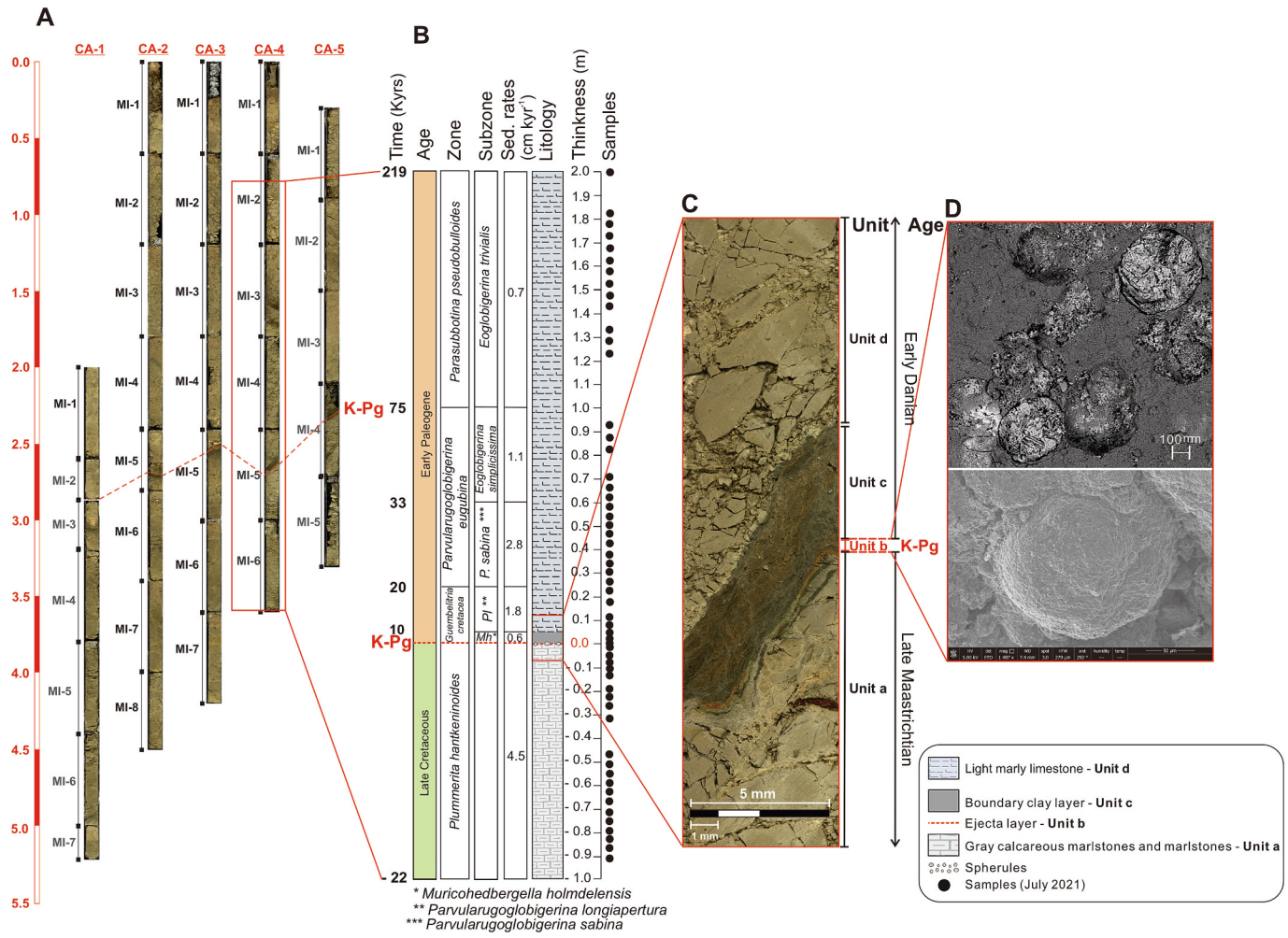

Fig. 2. (A) Photographs of 5 cores taken at the Caravaca section (dashed red line marks the K-Pg boundary). (B) Stratigraphic column of K-Pg boundary Caravaca section showing sample depths [black circles]). The ~3.0 m thick profile comprises 1.0 m of uppermost Cretaceous (unit a) and 2.0 m of Paleogene sediment; the latter includes an ejecta-rich layer (unit b), which contains spherules and an iridium anomaly, overlain by 6–10 cm of the blackish-gray boundary clay layer (unit c) and 1.90 m of the light marly limestones (unit d). (C) Detail of the K-Pg boundary recovered core. (D) High Resolution Scanning Field Scanning Electron Microscope (HRSEM) photographs of the impact spherules at the ejecta layer. (For interpretation of the references to colour in this figure legend, the reader is referred to the web version of this article.)

TOC concentration was determined by subtracting the inorganic carbon (IC) from the total carbon (TC) content in each sample, both determined with a SHIMADZU TOC-VCSH at the Stable Isotope Laboratory (SIDI) at the Universidad Autónoma de Madrid (Spain), with a precision better than 0.05%.

3.4.2. *Biomarker analysis*

A total of 65 samples were taken for biomarker analyses. They were extracted and analysed at the Organic Geochemistry Unit (OGU) at the University of Bristol (UK). Approximately 30 g of sediment was freeze-dried, then powdered using a steel ball mill (MM400) and extracted via a Soxhlet apparatus for 48 h using dichloromethane (DCM)/methanol (MeOH) (2:1 *v*/v). Then, total lipid extracts (TLE) were separated into two fractions using a column packed with activated silica by elution with hexane/DCM (9:1 v/v; apolar fraction) and DCM/MeOH (1:2 v/v; polar fraction). Finally, all fractions were evaporated to dryness under a steady flow of nitrogen.

GC analyses were performed on a CarloErba Gas Chromatograph equipped with a flame ionisation detector (FID) and fitted with a Chrompack fused silica capillary column (50 m × 0.32 mm interior diameter) coated with a CP Sil-5CB stationary phase (dimethylpolysiloxane equivalent, 0.12 μm film thickness). GC–MS analysis was performed on a Thermo Finnigan Trace Gas Chromatograph interfaced with a Thermo Finnigan Trace Mass Spectrometer operating with an electron ionisation source at 70 eV and scanning over *m/z* ranges of 50 to 850 Da. The GC was fitted with a fused silica capillary column (50 m × 0.32 mm i.d.) coated with a ZB1 stationary phase (dimethylpolysiloxane equivalent, 0.12 μm film thickness) and helium as the carrier gas. For both GC and GC–MS, 1 μl of sample was injected at 70 °C (1 min hold) using an on-column injector. The temperature was increased to 130 °C with an initial ramp of 20 °C/min, then to 300 °C at 4 °C/min, followed by an isothermal hold for 20 min. Due to the low concentration of the hopanes and steranes they were measured by SIM mode. All concentration results are semi-quantitative, with peak areas determined from appropriate mass chromatograms (*n*-alkanes *m/z* 57; hopanes *m/z* 191; steranes *m/z* 217 + 218) and normalized to the internal standard (5α-androstane) and amount extracted; due to varying response factors, these were not converted into absolute concentrations and we instead normalise the dataset to the sample with the highest concentration or mass accumulation rate as relevant (see below at 3.6).

3.5. *Stable isotope analyses*

The organic ($\delta^{13}C_{org}$) and inorganic ($\delta^{13}C_{carb}$) carbon and oxygen

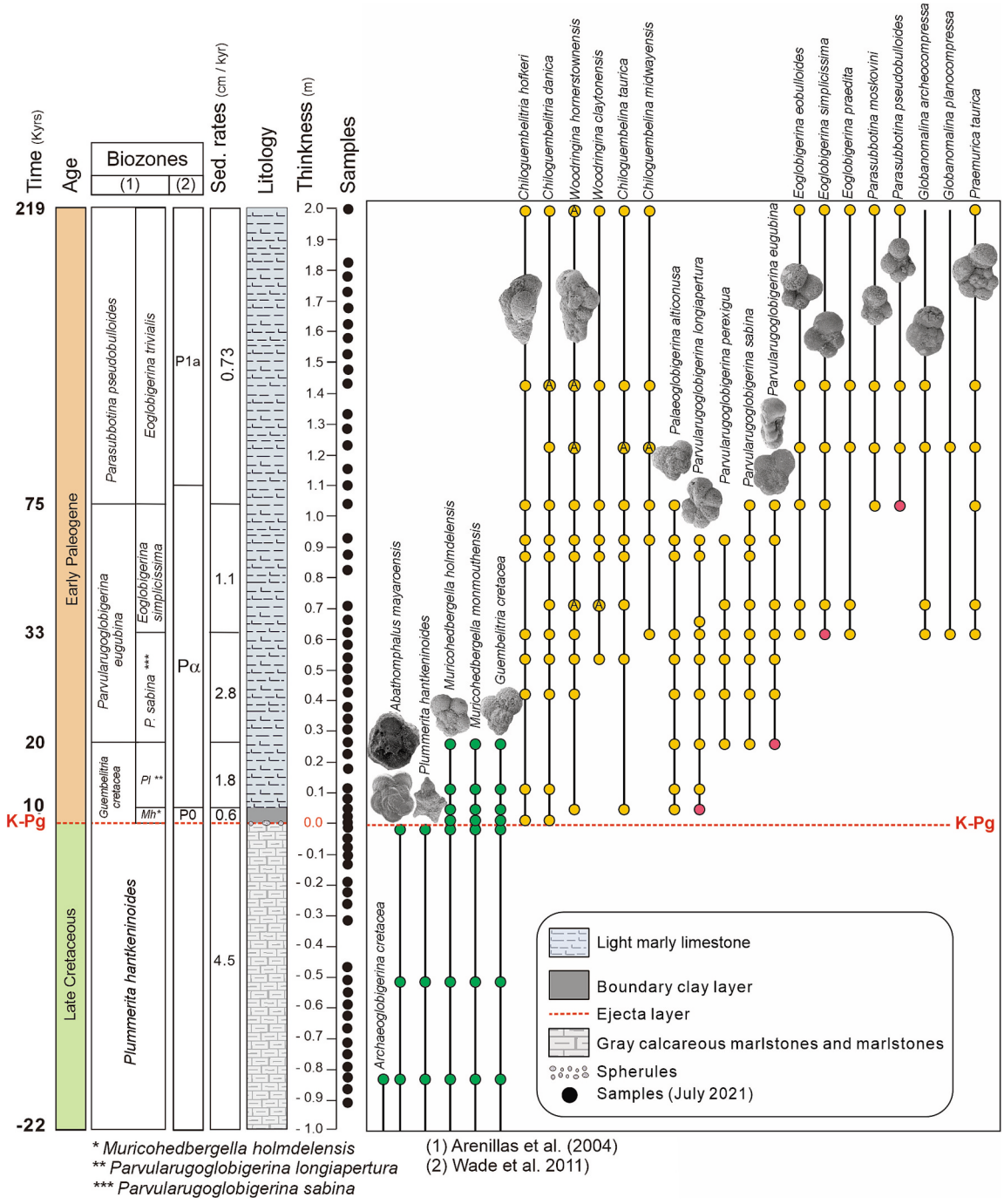

Fig. 3. Biostratigraphy of the Caravaca K-Pg section. For lithology, see caption in Fig. 2.

isotopes ($\delta^{18}O_{carb}$) were analysed in 65 samples from 1.0 m below to 2.0 m above the K-Pg boundary (21 samples on unit a, 1 sample unit b, 2 samples unit c, and 41 samples unit d). Analyses were conducted in the Stable Isotope Laboratory (SIDI) at the Universidad Autónoma de Madrid (Spain) ($\delta^{13}C_{org}$) and the Centro de Instrumentación Científica (CIC) from Universidad de Granada (Spain) ($\delta^{13}C_{Carb}$). For the former, inorganic carbon (IC) was removed, and all samples were weighed (between 0.012 and 0.030 g); depending on the quantity of total carbon (TC), they were then analysed with an elemental analyzer, a Carlo Erba 1108 coupled to a IRMS VG Isochrom, in continuous flow mode for bulk organic matter isotopic ($\delta^{13}C_{org}$) determination. The reference material used for $\delta^{13}C$ analysis was IA-R001 [$\delta^{13}C_{V\text{-}PDB} = -26.43‰$], with a precision better than 0.08‰. Results are expressed in the common δ-notation in per mil (‰) relative to the V-PDB standard. For determination of bulk inorganic carbon isotopic ($\delta^{13}C_{carb}$) and oxygen isotopic values ($\delta^{18}O$), all samples were treated with phosphoric acid (H_3PO_4 at 103%) using a VG Isocarb system thermostatized at 90 °C. The liberated CO_2 was analysed with an Isotope Ratio Mass Spectrometer (IRMS) VG Prism II. The international carbonate standard NBS-19 (National Bureau of Standards; $\delta^{13}C = 1.95‰$ and $\delta^{18}O = -2.20‰$) was used to calibrate to Vienna Pee Dee Belemnite (VPDB), with an average precision of 0.03‰ for $\delta^{13}C_{carb}$ and 0.05‰ for $\delta^{18}O$ analyses.

Stable carbon isotopic compositions of *n*-alkanes were determined for 30 samples, from 0.8 m below to 1.0 m above the K-Pg boundary (16 samples on unit a, 1 sample unit b, 1 samples unit c, and 12 samples unit d). This was done via gas chromatography-combustion-isotope ratio

mass spectrometry (GC-C-IRMS), at the OGU, University of Bristol, using a Hewlett Packard 6890 gas chromatograph connected to a Thermoquest Finnigan Delta plus XL spectrometer, via a GC III combustion interface (comprising Cu, Pt and Ni wires within a fused alumina reactor at a constant temperature of 940 °C). Duplicate analyses were conducted for each sample, with values reported in standard delta (‰) notation relative to Vienna Pee Dee Bee Belemnite (VPDB). Analytical accuracy, on the basis of replicate analysis of a standard of mixed fatty acid methyl esters (FAMEs), was typically ±0.5‰ and precision, represented by 1 standard deviation is generally < ±0.5‰.

3.6. Mass accumulation rates

Given the changes in lithology as well as likely changes in sedimentation rates (Gilabert et al., 2021, see at 4,1) across our section, we calculated Mass Accumulation Rates (MAR; μg/cm^2/kyr) to examine variations in OM input in relation to the time of deposition for different apolar biomarkers. The MAR was obtained by multiplying the concentration (μg/g Dry Weight) of each biomarker (pristane, phytane, *n*-alkanes, hopanes and steranes) by the sedimentation rates (cm^2/kyrs) calculated in each unit or foraminifera subzones (see at 3.2 and Fig. 4). Because concentrations are semi-quantitative, as discussed above, we then normalized MARs for each compound or class to the sample with the highest value which is set as MAR = 1.

4. Results

4.1. Biostratigraphy, age-depth model and sedimentation rate

Below the K-Pg boundary (unit a), a typical upper Maastrichtian association was recognized, where *Plummerita hantkeninoides* is present and whose last occurrence marks the upper boundary of the biozone of the same name and the top of the Cretaceous. The upper part of the section (200 cm above the K-Pg boundary) is represented by the biozones of *Guembelitria cretacea*, *Parvularugoglobigerina eugubina* and the lower part of *Parasubbotina pseudobulloides*. The *Gb. cretacea* biozone has been divided into two subzones on the basis of the lowest occurrence (LO) of *Parvularugoglobigerina longiapertura* (Arenillas and Arz, 2000). The 6 cm interval located directly above the K-Pg boundary (Fig. 3), which includes the reddish ejecta level and the dark boundary clay layer (units b and c), contains the assemblage formed by *Muricohedbergella holmdelensis*, *Muricohedbergella monmouthensis*, *Heterohelix globulosa*, *Guembelitria cretacea*, *Guembelitria blowi*, *Chiloguembelitria hofkeri*, *Chiloguembelitria danica* and Pseudocaucasina antecesor. This association characterises the *M. holmdelensis* subzone, equivalent to the Zone P0 of Berggren and Pearson (2005) and Wade et al. (2011). Reworked Cretaceous specimens are abundant in this subzone. At the base of unit d (Fig. 3), 9 cm above the K-Pg boundary (sample CA4–5-Pg 6–9, Table 1 from Supplementary material), the first trochospiral forms represented by tiny parvularugoglobigerids (*Parvularugoglobigerina* and *Palaeoglobigerina*) appear, which was used to place the base of the *Pv. longiapertura* subzone.

The LO of *Parvularugoglobigerina eugubina* in a sample situated 24 cm above the K-Pg boundary (CA4–4-Pg-24-28, Table 1 from Supplementary material), marks the base of the biozone of the same name. Within this biozone, the subzones *Parvularugoglobigerina sabina* and *Eoglobigerina simplicissima* can be identified. The first subzone covers a range of 36 cm, from 24 to 60 cm above K-Pg (samples CA4–4-Pg-24-28 to CA4–4-Pg-56-60, Table 1 from Supplementary material) and is characterised by an abundance of *Parvularugoglobigerina* taxa. The LO of *Eoglobigerina* species with a pitted/cancellate wall texture (Arenillas et al., 2004; Arenillas and Arz, 2013) occurs 60 cm above the K-Pg boundary (sample

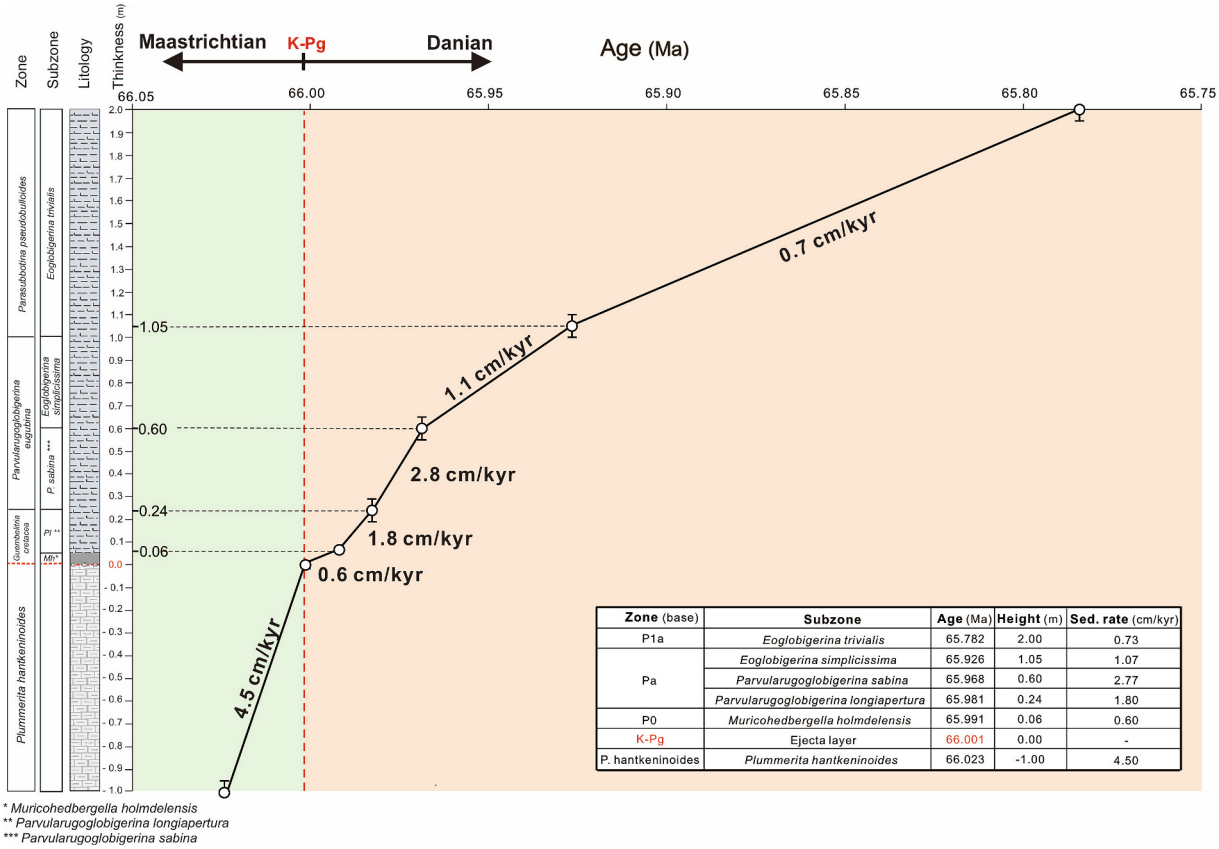

Zone (base)	Subzone	Age (Ma)	Height (m)	Sed. rate (cm/kyr)
P1a	*Eoglobigerina trivialis*	65.782	2.00	0.73
Pa	*Eoglobigerina simplicissima*	65.926	1.05	1.07
	Parvularugoglobigerina sabina	65.968	0.60	2.77
	Parvularugoglobigerina longiapertura	65.981	0.24	1.80
P0	*Muricohedbergella holmdelensis*	65.991	0.06	0.60
K-Pg	Ejecta layer	66.001	0.00	-
P. hantkeninoides	*Plummerita hantkeninoides*	66.023	-1.00	4.50

Fig. 4. Age-depth model plot for our Caravaca K-Pg section based on Arenillas et al. (2004) and Gilabert et al., 2021. Sedimentation rates are shown next to segments of the age model line. For lithology, see caption in Fig. 2. For K-Pg boundary age we used Gradstein et al. (2020).

CA4–4-Pg-60-64, Table 1 from Supplementary material). This bioevent and the abundance of *Woodringina* are used to identify the *E. simplicissima* subzone. According to Berggren and Pearson (2005) and Wade et al. (2011), the Zone Pα represents the interval of total range of *Pv. eugubina*. Following the arguments of Arenillas and Arz (2000), Arenillas et al. (2004) and Metsana-Oussaid et al. (2019), the Zone Pα comprises the *Pv. longiapertura* subzone, *Pv. eugubina* biozone and the lowest *Parasubbotina pseudobulloides* biozone (Fig. 3).

The last 95 cm of the Caravaca section belong to the *P. pseudobulloides* biozone, defined by the first occurrence of the index species. In addition, this biozone is characterised by the predominance of *Chiloguembelitria* and *Woodringina*, together with other less frequent species as *Parasubbotina*, *Eoglobigerina*, *Chiloguembelina*, *Globanomalina* or *Praemurica* (Fig. 3 and Table 1 from Supplementary material). The absence of *Subbotina triloculinodes* in the samples indicates that only the *Eoglobigerina trivialis* subzone is represented in this section. This subzone is practically equivalent to the Subzone P1a of Berggren and Pearson (2005) and Wade et al. (2011).

Biostratigraphic analysis revealed frequently reworked Cretaceous specimens in the lower part of the Danian, until 0.3 m above the K-Pg boundary, particularly abundant in the initial samples (P0). The existence of reworked Cretaceous specimens in the Danian of the Caravaca section was previously demonstrated by Kaiho and Lamolda (1999). Recently, Gilabert et al. (2021) studied the palaeoenvironmental changes of the lower Danian of Caravaca and identified numerous Cretaceous specimens reworked in the earliest Danian samples. Additionally, a significant decline in the abundance of reworked Cretaceous specimens was observed throughout the lower part of the Danian, a trend also documented by Arz et al. (2000). On the other hand, the identification of all biozones and subzones defined for the K-Pg transition suggests that in this section there were no hiatuses and implies stratigraphic continuity.

Utilizing the planktonic foraminifera biohorizons previously calibrated by Arenillas et al. (2004) and Gilabert et al. (2021) as a reference, we estimated the following age-depth model for the Caravaca CA4 core from the Caravaca K-Pg section (see Fig. 4). The samples stratigraphically underlying the K-Pg boundary (from −1.00 m to the K-Pg boundary) do not record any distinct first or last occurrence biohorizon. However, the entire assemblage is characterised by planktonic foraminifera indicative of the latest Maastrichtian *P. hantkeninoides* Biozone (Arenillas et al., 2004). The Lowest Occurrence (LO) of the index taxon, a bioevent dated by Husson et al. (2014) as 140 kyr prior to the K-Pg boundary, was used as a chronostratigraphic tie-point. Leveraging this tie-point, Gilabert et al. (2021) established an average sedimentation rate of 4.5 cm/kyr for the latest Maastrichtian interval within the Caravaca section. Assuming a constant sedimentation rate of 4.5 cm/kyr across at the uppermost Cretaceous, we propose an approximate duration of 22.2 kyr for our uppermost Maastrichtian sedimentary sequence. The ejecta layer represents an extremely rapid deposition event, potentially occurring over a timescale of years to decades (Artemieva and Morgan, 2020; Artemieva and Morgan, 2009), but the boundary clay layers have low sedimentation rates (P0; 0.6 cm/kyr). Then sedimentations rates increase from 1.80 to 2.77 cm/kyr, and finally decrease again to 1.07 cm/ky and 0.73 cm/kyr in the top of our studied section.

4.2. Core scan profiles

Geochemical data analysed by XRF core scanner are presented as elemental ratios (Ca/Al, Ba/Al, K/Al, Ti/Al and Ir and $CaCO_3$ [%]) across the K-Pg boundary (Fig. 5). Selected Al-normalized ratios provide

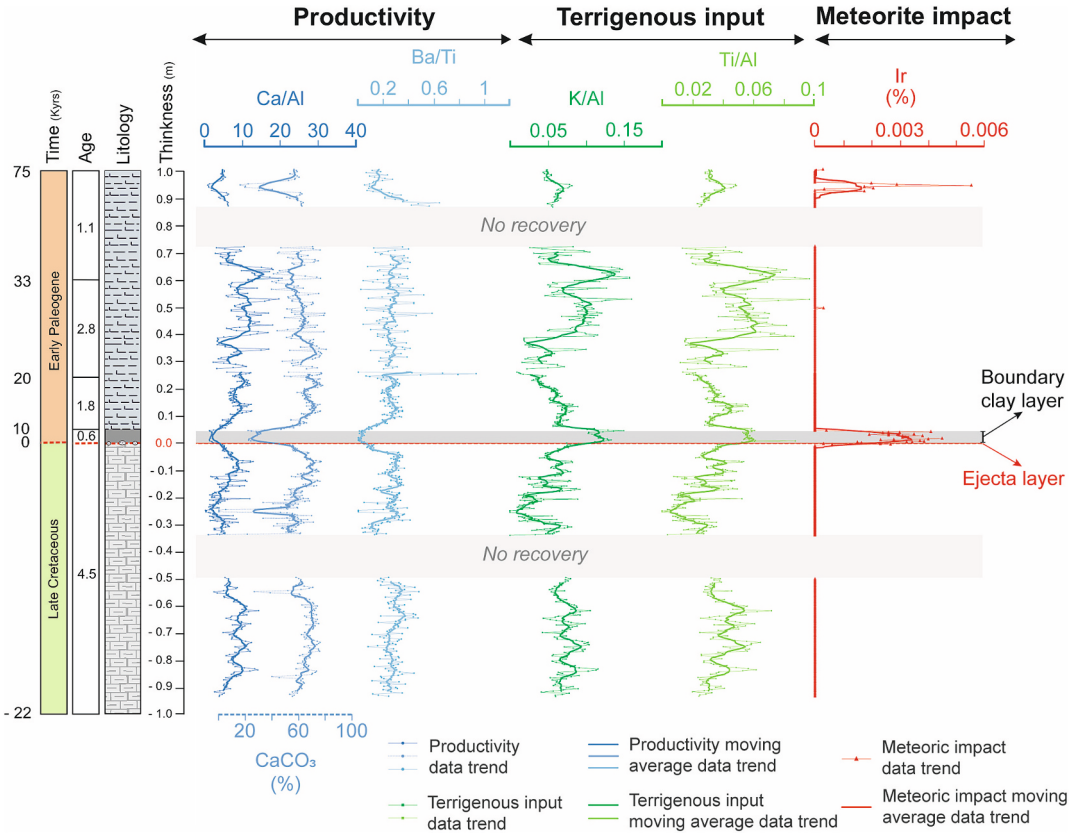

Fig. 5. Inorganic XRF core scanner profiles, showing: **(A)** Productivity ratios, such as Ca/Al (continuous dark blue line), Ba/Ti (dashed light blue line) and $CaCO_3$ content (%, continuous light blue line); **(B)** terrigenous input ratios, such as K/Al (continuous dark green line) and Ti/Al (continuous light green line); and **(C)** the meteoric impact ratio Ir (continuous red line). For lithology, see caption in Fig. 2. For interpretation of the references to colour in this figure legend, the reader is referred to the web version of this article. (For interpretation of the references to colour in this figure legend, the reader is referred to the web version of this article.)

information about environmental variations at continuous, mm-resolution along the ~200 cm-thick studied interval (100 cm above and below K-Pg boundary). Elemental ratios related to the extraterrestrial input, such as Ir, all clearly identify the ejecta layer (Fig. 5C). Although the XRF core scanner instrument is not the best option to make accurate Ir analyses, Ir was only detected at the ejecta layer and was below detection in all other samples. Some geochemical ratios used as productivity indicators, such as Ca/Al, Ba/Ti, and $CaCO_3$ content (%) decrease within the ejecta layer and boundary clay layer, with minimum values of ~5 for the Ca/Al ratio, ~0.1 for the Ba/Ti ratio and ~ 15% for the % $CaCO_3$ content (Fig. 5). Typical detrital input ratios, K/Al and Ti/Al, have more complex profiles, with several peaks in the early Paleocene but also during the ejecta layer and boundary clay layer deposition.

4.3. Stable isotopes

The $\delta^{18}O$ profile shows some variability along the section, with values ranging between −1.04 and −2.28‰ (Fig. 6B). A clear $\delta^{18}O$ negative excursion is recorded at the K-Pg, with a negative shift of 2.0‰, and a later recovery at ca. 8 cm above the K-Pg. Values from 8 to 100 cm above the K-Pg boundary (ejecta and clay boundary layers) are similar to those of the Cretaceous and then increase to the top of the unit d.

The $\delta^{13}C_{carb}$ profile also shows variability along the section, with values ranging between 0.07 and 2.05‰ (Fig. 6C). A clear negative excursion in $\delta^{13}C_{carb}$ of 1.5‰ is recorded just at the ejecta and boundary clay layers, recovering to pre-excursion values ca. 8 cm above the K-Pg. Another 1.0‰ negative excursion is observed between 90 cm to 125 cm above the K-Pg. Otherwise, values are very similar for the Cretaceous, the first meter above K-Pg and between 1.4 and 2.0 above K-Pg. The $\delta^{13}C_{org}$ values show more variability and range between −24.4 and −27.6‰ (Fig. 6C). Positive excursions are observed at 50 cm below the K-Pg and between 90 cm to 125 cm above K-Pg. The $\delta^{13}C_{org}$ profile also exhibits a positive rather than negative carbon isotope excursion (with a positive shift of 2.0‰) in both the ejecta layer and in the boundary clay layer above K-Pg.

To further explore the organic carbon isotopic signature, we determined $\delta^{13}C$ values of high-molecular-weight (HMW) odd-carbon-number *n*-alkane (>*n*-C_{29}; Fig. 6D). These could preferentially reflect higher plant signals via a leaf wax origin (Eglinton and Hamilton, 1967), but that interpretation is complicated in thermally mature samples where *n*-alkanes may derive from multiple sources. The mean-weighted $\delta^{13}C_{HMW}$ value for the uppermost Cretaceous (unit a) is −29‰, although it decreases upwards from −28‰ to −31‰, before increasing just prior to the ejecta layer. The ejecta layer itself (unit b) contains a single sample

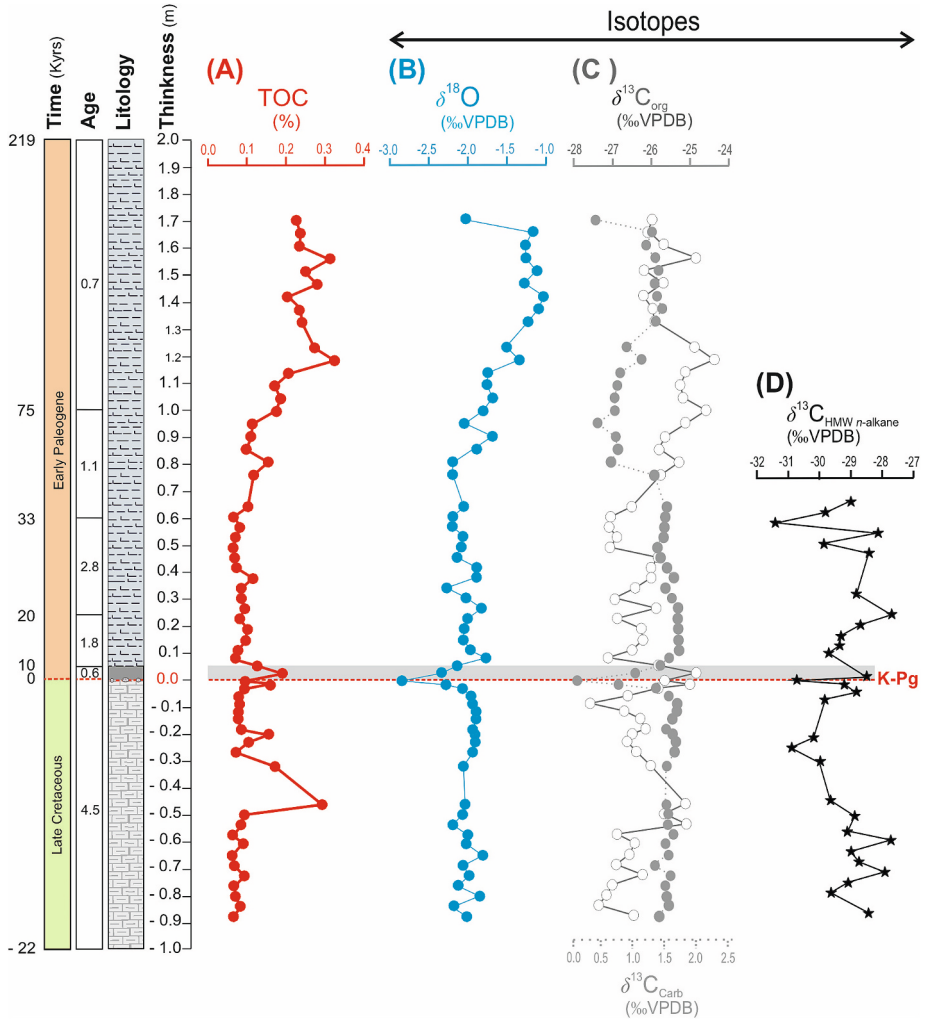

Fig. 6. TOC contents (A; continuous red line) and carbon isotopic data at the Caravaca K-Pg section, including: (B) Oxygen isotopic compositions of bulk carbonate ($\delta^{18}O$-continuous blue line). (C) Carbon isotopic compositions of bulk organic carbon ($\delta^{13}C_{org}$-continuous gray line and open circles) and inorganic carbon ($\delta^{13}C_{Carb}$-dashed gray line and solid circles); and (D) Carbon isotopic compositions of high molecular weight *n*-alkanes ($\delta^{13}C_{HMW}$-continuous black line). For lithology, see caption in Fig. 2. For interpretation of the references to colour in this figure legend, the reader is referred to the web version of this article. (For interpretation of the references to colour in this figure legend, the reader is referred to the web version of this article.)

with a $\delta^{13}C_{HMW}$ value of −31‰. Then, at the clay boundary (unit c) and until the first 60 cm from the Danian (unit c, ~33 kyr after the K-Pg), $\delta^{13}C_{HMW}$ values are variable around −29‰. Finally, in the upper part, at 62.5 cm above the K-Pg boundary (~35 kyr after the K-Pg) $\delta^{13}C_{HMW}$ values again decrease to −31.1‰. Some of these trends parallel those of $\delta^{13}C_{org}$, but others are markedly distinct including a negative rather than positive excursion in the ejecta layer.

4.4. TOC content

TOC content is less than 1% throughout the section (Fig. 6A), varying from 0.14 to 0.89%. In unit a from the late Cretaceous, it ranges from 0.14% to 0.67% (mean value of 0.22%). In the early Paleogene, values are 0.37% at the ejecta layer (unit b), from 0.22% to 0.44% (mean value of 0.33%) at the boundary clay layer (unit c) until 10 kyrs after the K-Pg, from 0.15% to 0.27% (mean value of 0.22%) within the unit d until ~75 kyrs after the K-Pg, and from 0.39% to 0.89% (mean value of 0.57%) until ~220 kyrs after the K-Pg (Fig. 6A).

4.5. Biomarkers

Despite relatively low TOC contents (Fig. 6A), the sediments from Caravaca K-Pg boundary sections contain diverse hydrocarbons (Fig. 7) from both terrestrial and marine sources (e.g. *n*-alkanes, acyclic isoprenoids, steranes, hopanes).

The apolar compounds' distributions and concentrations vary stratigraphically through the section (Fig. 8). These include a homologous series of *n*-alkanes (Fig. 7, red colour) with a low but variable odd-over-even predominance (expressed as the carbon preference index, which varies from ~1 to 3; Fig. 8), suggesting a significant terrigenous input of OM to the sediments (Cranwell et al., 1987; Eglinton and Clavin, 1967; Eglinton and Hamilton, 1967b; Kvenvolden, 1967; Rieley et al., 1991). In many samples, the distribution of *n*-alkanes is bimodal with a significant amount of mid-molecular-weight *n*-alkanes (Fig. 7). LMW *n*-alkanes ($\leq C_{21}$), typically attributed to aquatic algal and bacterial sources (Cranwell et al., 1987; Schneider et al., 1970) are present in low abundances throughout (<10% of the total *n*-alkanes, Fig. 8), although they represent a slightly higher proportion of the *n*-alkanes just at the ejecta and boundary clay (unit b and c). Other biomarkers occur in only very low concentrations, typically at the limit of detection (Fig. 7). Pristane and phytane (Fig. 7, orange colour) are present in concentrations similar to those of co-occurring LMW *n*-alkanes and exhibit minimal changes across the section. The apolar fractions also contain a series of bacterially derived C_{27} to C_{31} hopanes (Fig. 7, blue colour), as well as eukaryote derived C_{27}-C_{29} regular steranes (Fig. 7, purple colour).

4.5.1. Depth profiles of biomarkers

Many of the biomarkers and biomarker ratios can constrain OM sources (marine, terrestrial or reworked) as well as the thermal maturity of the OM in the Caravaca section. Evidence for marine OM input is suggested by the pristane and phytane and LMW/total *n*-alkane ratios ($[C_{17} + C_{18} + C_{19} + C_{20} + C_{21}] / [\sum$ total *n*-alkane]; Cranwell et al., 1987; Eglinton and Hamilton, 1967), and possibly by high proportions (%) of C_{27} steranes (e.g., Huang and Meinschew, 1979) (Fig. 8A). LMW/total *n*-alkane ratios (Cranwell et al., 1987; Eglinton and Hamilton, 1967) are always low but highest at 10 cm below K-Pg boundary, and at

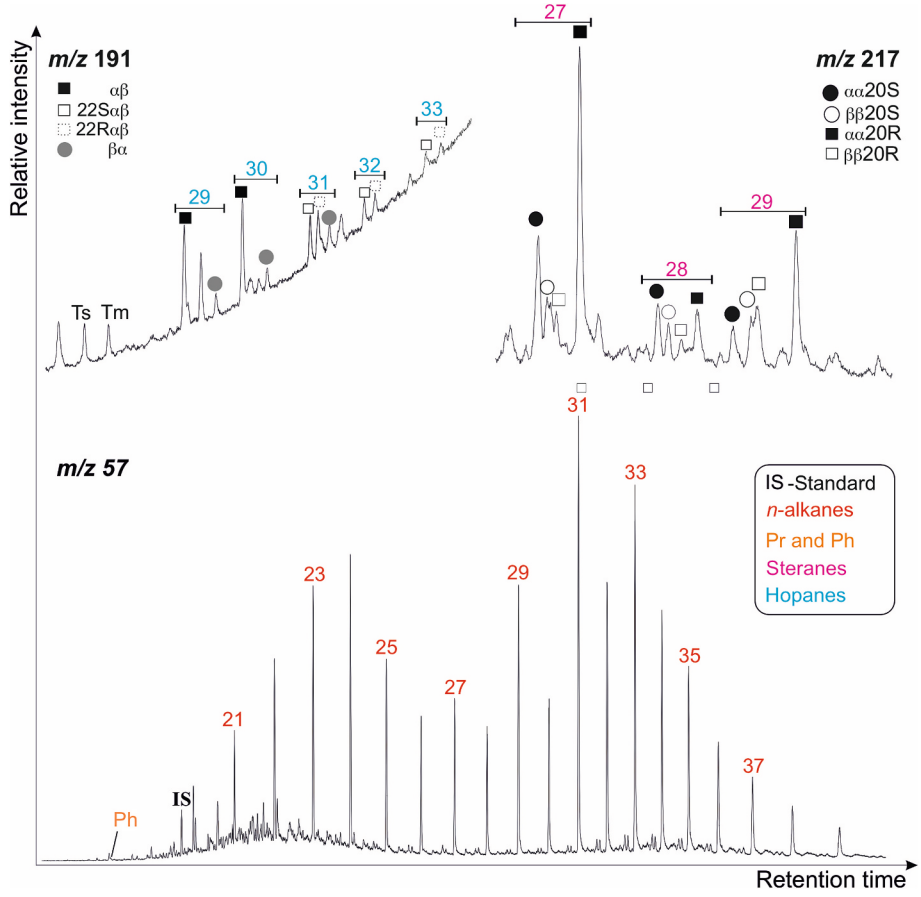

Fig. 7. Apolar fractions from Caravaca K-Pg boundary section. The *m/z* 57 mass chromatogram showing predominantly *n*-alkanes (red colours), Pr = pristane and Ph = phytane (orange colour). Numbers correspond to carbon chain length. IS = internal standard (5α-androstane). Hopanes occur in low concentrations and are shown by the *m/z* 191 mass chromatogram (blue colours). Steranes are shown by the *m/z* 217 mass chromatogram (purple colours). (For interpretation of the references to colour in this figure legend, the reader is referred to the web version of this article.)

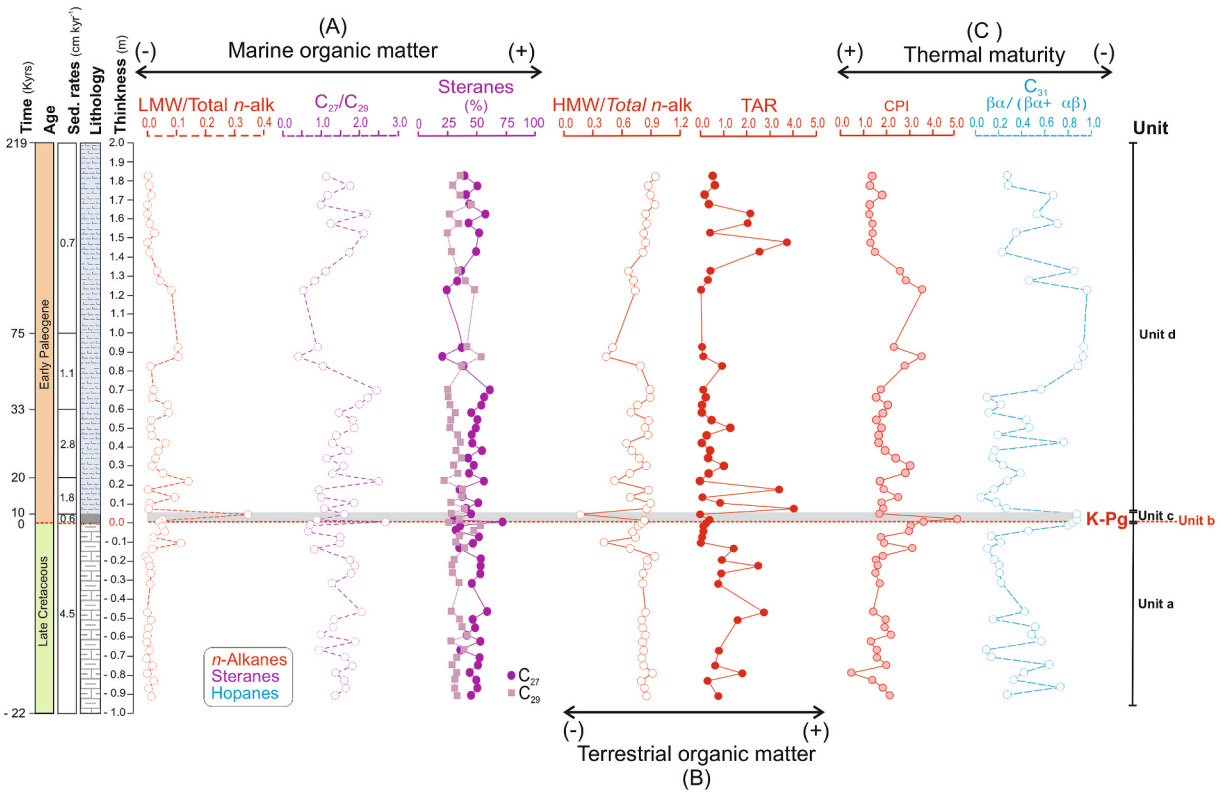

Fig. 8. Biomarker profiles through the Caravaca K-Pg section. **(A)** Biomarker ratios related to marine OM input, including LMW *n*-alkane/∑total *n*-alkane ratio (discontinuous red line); C_{27}/C_{29} sterane ratio (discontinuous purple line) and % of C_{27} and C_{29} regular steranes [C_{27}/ Σ(C_{27} + C_{28} + C_{29}) - continuous dark purple line and C_{29}/ Σ(C_{27} + C_{28} + C_{29}) - discontinuous light purple line]. **(B)** Biomarker ratios related to terrestrial OM input, including HMW *n*-alkane/∑total *n*-alkane ratio (continuous red line); terrigenous/aquatic ratios (TAR) of *n*-alkanes (continuous red line) **(C)** Biomarker ratios that can be related with thermal maturity: CPI of *n*-alkanes (continuous red line and light red circles) and C_{31} βα/(βα + αβ) hopane ratio (blue dashed line). The K-Pg boundary is indicated by the horizontal red dash line. The black arrow shows higher and lower OM input and thermal maturity. For lithology, see caption in Fig. 2. For interpretation of the references to colour in this figure legend, the reader is referred to the web version of this article. (For interpretation of the references to colour in this figure legend, the reader is referred to the web version of this article.)

4.5 cm, 20 cm and 100 cm above the K-Pg boundary (Fig. 8A); and the C_{27}/C_{29} sterane ratio shows a similar trend (Fig. 8A). The putative algal chlorophyll degradation products, pristane and phytane (Dean and Whitehead, 1961; Rontani and Volkman, 2003), are present through all the Caravaca CA4 core except in the ejecta layer (unit b) (Figs. 7 and 9B). The C_{27} sterane proportions (%) are higher than C_{29} (%) throughout the entire section except a few cm below and between 90 and 125 cm above the K-Pg boundary (e.g., Huang and Meinschew, 1979) (Fig. 8A).

Evidence for terrestrial OM input is suggested by high abundances of long-chain *n*-alkanes with an odd-over-even predominance, reflected by HMW/ total *n*-alkane ratios ([C_{27} + C_{28} + C_{29} + C_{30} + C_{31} + C_{32} + C_{33} + C_{34} + C_{35} + C_{36} + C_{37}] / [∑ total *n*-alkane]) (Cranwell et al., 1987; Eglinton and Hamilton, 1967), terrestrial to aquatic ratios (TAR; [C_{27} + C_{39} + C_{31}] / [C_{15} + C_{17} + C_{19}]) (Bourbonniere and Meyers, 1996; Cranwell et al., 1987), and possibly by high proportions (%) of C_{29} steranes (e.g., Huang and Meinschew, 1979) (Fig. 8B). In our section, HMW/total *n*-alkane ratios have two minima at 10 cm below and 4.5 cm above the K-Pg. TARs have maximum values at the bottom of the unit d, between 6 and 20 cm above K-Pg. C_{29} steranes (%) are generally less abundant than C_{27} steranes (%), except for a few cm below and between 90 and 125 cm above the K-Pg boundary, which could indicate increased terrigenous input at those intervals (Fig. 8B). However, the steranes trends are dissimilar to those of the *n*-alkanes (Figs. 8–9), suggesting that the former reflect variations in algal sources (i.e. Schwark and Empt, 2006) rather than terrestrial/marine sources.

The diagenetic alteration and thermal maturity OM ratios calculated here, i.e. the Carbon Preference Index (CPI = $1/2*\Sigma(X_i + X_{i+2} + \ldots + X_n)/\Sigma(X_{i-1} + X_{i+1} + .. + X_{n-1}) + 0.5*\Sigma(X_i + X_{i+2} + \ldots + X_n)/ \Sigma(X_{i+1} + X_{i+3} + \ldots + X_{n+1})$, with $i = 25$ and $n = 35$) (Bray and Evans, 1961; Peters et al., 2005) and the C_{31} βα / (αβ + βα) hopane ratio, both show that the Caravaca K-Pg section is thermally mature but not overmature. Consequently, functionalized biomolecules such as glycerol dialkyl glycerol tetraether lipids (GDGTs, Schouten et al., 2013), are not detected nor are the biologically produced and thermally unstable 17β(H),21β-homohopane (C_{31}ββ hopane) and 17β(H),21β hopane (C_{30}ββ hopane) isomers (Mackenzie et al., 1980; Ourisson et al., 1979; Peters and Moldowan, 1991; Seifert and Moldowan, 1980). Consistent with that, the $C_{27–29}$ sterane compounds are represented by their four epimers (5α(H),14α (H),17α(H),20R; 5α(H),14α (H),17α(H),20S; 5α(H),14β(H),17β(H),20S and 5α(H),14β(H),17β(H),20R).

Variations in thermal maturity parameters through the section likely reflect changes in source inputs (e.g. Bray and Evans, 1961; Peters et al., 2005). The CPIs, which typically approach 1 in thermally mature rocks (e.g. Gearing et al., 1976; Pendoley, 1992), are particularly high (close to ~5) in the ejecta layer (unit b) and at the bottom of the boundary clay layer (unit c). The C_{31} hopane ratio [17β(H),21α / (17β(H),21α + 17a (H),21β)]–hereafter βα / (βα + αβ), which decreases with thermal maturity, is low (~0.3) through most of the section but reaches a maximum value ~0.8 for both, the ejecta (unit b) and boundary clay (unit c) layers (Fig. 8C). The CPI and βα/(βα + αβ) ratios could reflect reduced reworking of older, thermally mature OM, in contrast to observations at other K-Pg sites (Sosa-Montes de Oca et al., 2024). However, alternative explanations exist for both. The CPIs could reflect the input of less diagenetically altered, i.e. 'fresher' OM which has experienced shorter soil residence times (e.g. Bray and Evans, 1961; Peters et al., 2005). Moretane abundances (βα) are partially governed by

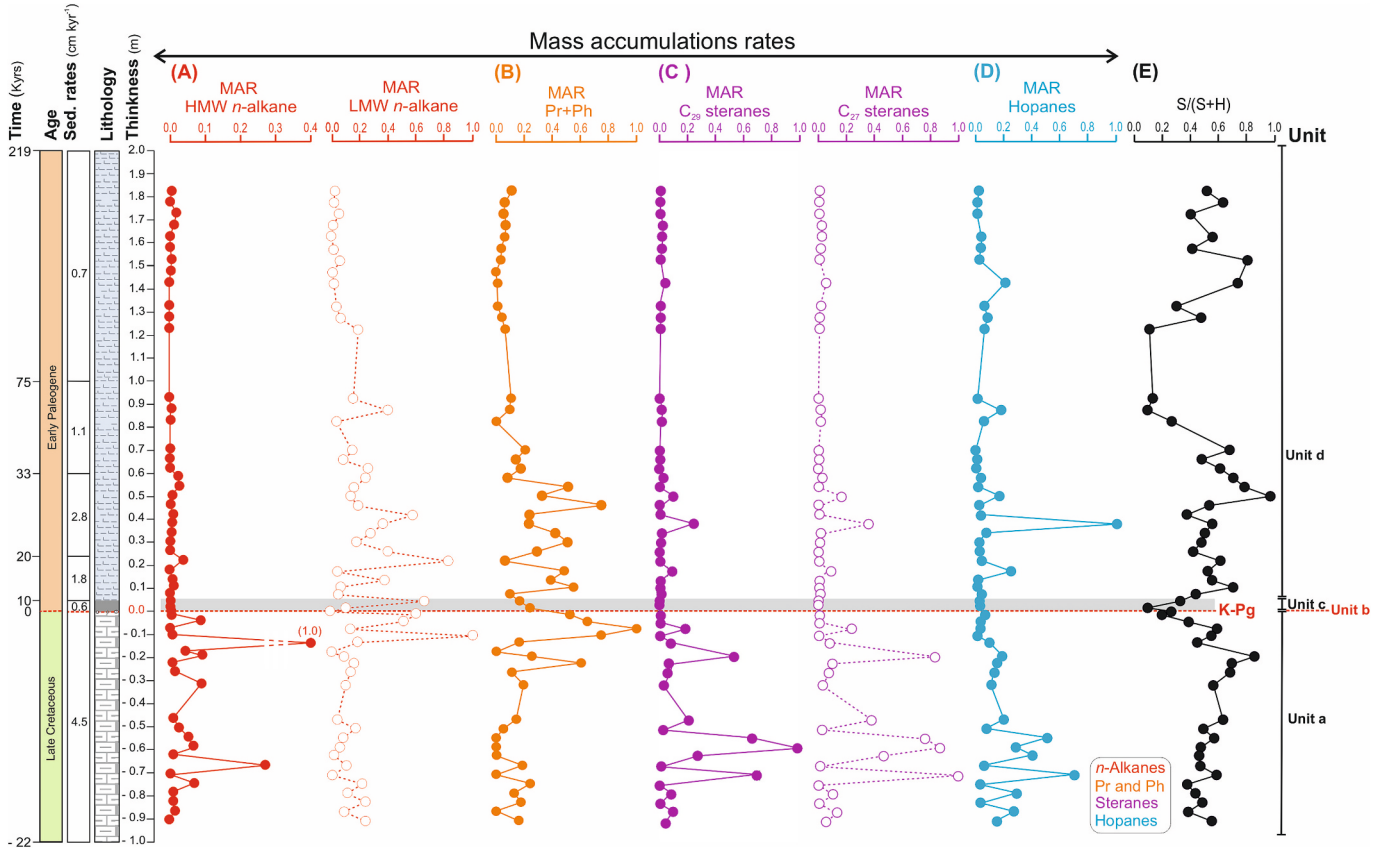

Fig. 9. Relative mass accumulation rates (normalized to each sample with highest abundance) of apolar biomarkers in the Caravaca section: (A) MAR HMW *n*-alkanes (continuous red line and solid circles) and MAR LMW *n*-alkanes (discontinuous red line and open circles); (B) MAR pristane (Pr) + phytane (pH) (continuous orange line); (C) MAR C_{29} steranes (continuous purple line and solid circles) and MAR C_{27} steranes (discontinuous purple line and open circles); and (D) MAR total hopanes (continuous purple line). Also shown is (E) the S/(S + H) ratio (continuous black line). We did not calculate MAR in the ejecta layer. For lithology, see caption in Fig. 2. For interpretation of the references to colour in this figure legend, the reader is referred to the web version of this article. (For interpretation of the references to colour in this figure legend, the reader is referred to the web version of this article.)

lithology and decrease with carbonate content (Peters et al., 2005), such that decreased carbonate deposition in the ejecta layer and lower boundary layer could explain the elevated βα / (βα + αβ) ratios.

4.6. *Relative mass accumulation rates profiles*

MAR was not calculated for the ejecta layer (unit b) because it was deposited rapidly, potentially on the order of days to months (Artemieva and Morgan, 2009) (Fig. 9). The MARs of *n*-alkanes (Fig. 9A), steranes (Fig. 9C) and hopanes (Fig. 9D) are all the highest in sediments from the Late Cretaceous (unit a) (Fig. 9). MARs for the same biomarkers are 3 to 4 times lower (or more) in the Paleogene sediments (units b-c). The differences in these values are partially but not entirely due to the lower sedimentation rates during the Paleogene. Overall, this suggests that the mass extinction was associated with decreased OM and carbonate production that persisted long after the event, in contrast to observations at other distal sites (Bralower et al., 2020; Hull and Norris, 2011; Lowery and Bralower, 2022; Sepúlveda et al., 2009; Sosa-Montes de Oca et al., 2023; Sosa-Montes de Oca et al., 2021). Alternatively, it could reflect poorer OM preservation with lower sedimentation rates (Aller, 1998). However, the acyclic isoprenoids pristane and phytane (Fig. 9B) exhibit markedly different trends, as do those of the LMW *n*-alkanes if they are disaggregated from the total *n*-alkane numbers (see Fig. 9A). The MARs of these compounds of putative marine origin increase in the latest Cretaceous and remain high but variable through the earliest Paleogene (unit c and lower unit d), similar to some central Pacific and Atlantic sites (Hull and Norris, 2011).

5. Discussion

The K-Pg mass extinction strongly impacted phytoplankton and calcareous nan noplankton communities (Alvarez et al., 2019; Lowery et al., 2020), but the response of non-fossilizing plankton remains less clear (Lowery et al., 2020). Until now, there are few studies based on biomarkers on the K-Pg boundary (Bralower et al., 2020; Sosa-Montes de Oca et al., 2021, 2023, 2024; Schaefer et al., 2020; Sepúlveda et al., 2009; Taylor et al., 2018). Here, we apply organic geochemistry analyses to evaluate how different OM sources (terrestrial, marine or reworked) changed before and after this mass extinction using a continuous 300-cm sequence (~242 kyr) of the Caravaca K-Pg distal section (SE Spain). First, we evaluate the isotopic and inorganic profiles to understand changes in paleoenvironmental conditions. We then explore changes in the relative contribution of terrigenous, marine and reworked OM (the latter inferred from changes in the thermal maturity of the biomarkers). Finally, we examine hopane, sterane, *n*-alkane and Pr + Ph distributions in greater detail, using those to explore the recovery of primary producers, mainly bacterial and non-fossilizing communities, after the K-Pg mass extinction.

5.1. *Changes in paleoenvironmental conditions*

Negative carbon isotope excursions (-CIEs) in both $\delta^{13}C_{carb}$ and $\delta^{13}C_{org}$ have been commonly observed, due to global collapse in export productivity (the flux of OM from the surface to deep ocean), in several post-K-Pg boundary intervals (Birch et al., 2016; Sepúlveda et al., 2019). Generally, at those distal sites (e.g., Ocean Drilling Program, ODP, site

1262 Walvis ridge; El Kef and Ain Settara in Tunisia; Bidart and Loya bay in France and Kulstirenden an Hojerup in Demark), the -CIEs in $\delta^{13}C_{org}$ are smaller and shorter than in $\delta^{13}C_{carb}$. However, in the distal Caravaca section an unexpected +CIE occurs in the $\delta^{13}C_{org}$ record (Fig. 6C), although not in the carbon isotopic compositions of the *n*-alkanes ($\delta^{13}C_{HMW}$; Fig. 6D). An unexpected +CIE was also observed in the $\delta^{13}C_{org}$ record of the Agost distal section (Spain) (Sepúlveda et al., 2019; Sosa-Montes de Oca et al., 2021) as well as in the Mid-Waipara K-Pg distal section (New Zealand) (Sosa-Montes de Oca et al., 2023) (Fig. 10). As for those previous studies, we attribute this discrepancy to the complex OM source changes across the K-Pg boundary, which can complicate both organic carbon and *n*-alkane carbon isotopic compositions. The impact of reworked OM on the fidelity of the bulk organic carbon isotopic record has been documented previously for other time intervals (Carmichael et al., 2019).

Therefore, we instead discuss changes in the carbon cycle recorded by HMW *n*-alkanes likely related to higher terrestrial plants ($\delta^{13}C_{HMW}$). These values are governed by the isotopic composition of substrate carbon, i.e. atmospheric CO_2 (Arens and Jahren, 2000; Popp et al., 1989), fractionation during carbon assimilation (ε_p) (Farquhar et al., 1989; Farquhar et al., 1982; Popp et al., 1989) and environmental conditions that influence ε_p values, such as water stress (e.g. Diefendorf et al., 2011; Diefendorf et al., 2010; Kohn, 2010). Both $\delta^{13}C_{carb}$ and $\delta^{13}C_{HMW}$ should have a similar trend, if both are governed primarily by changes in the carbon isotopic composition of atmospheric CO_2.

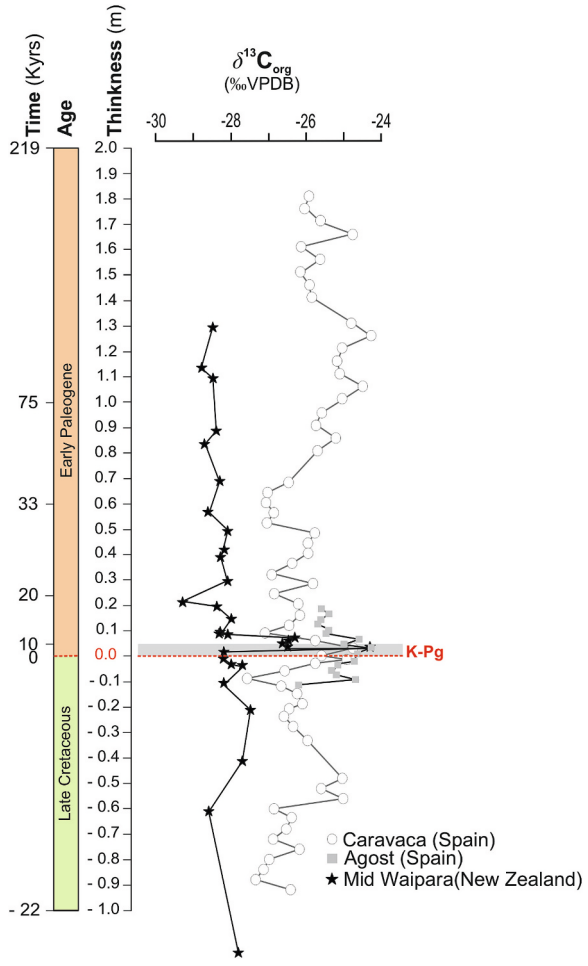

Fig. 10. Comparison of bulk organic carbon isotopic data ($\delta^{13}C_{org}$) at several K-Pg sections: the Caravaca section (open circles) and the Agost section (gray squares), both located in Spain, and the Mid Waipara section in New Zealand (solid stars). For interpretation of the references to colour in this figure legend, the reader is referred to the web version of this article.

However, the $\delta^{13}C_{HMW}$ values exhibit much more variability than the $\delta^{13}C_{carb}$ values, which are generally stable with the exception of the -CIE at the K-Pg boundary; this likely reflects secondary factors controlling $\delta^{13}C_{HMW}$ such as the impact of hydrology on ε_p values, changes in source vegetation, and contributions of reworked OM. The −2‰ CIE shift is similar in both $\delta^{13}C_{HMW}$ and $\delta^{13}C_{carb}$, and it was also detected in bulk terrestrial records from New Mexico, North Dakota, and Montana (Arens and Jahren, 2000; Beerling et al., 2001; Schimmelmann and DeNiro, 1984).

K-Pg carbon isotopic profiles ($\delta^{13}C_{carb}$, $\delta^{13}C_{org}$ and $\delta^{13}C_{HMW}$) are rather geographically variable, but some of the features of the Caravaca section have been observed elsewhere. The ~1–2‰ positive shift, in $\delta^{13}C_{org}$ prior to the K-Pg boundary (unit a), at −10 cm equivalent to ~2.5 kyr before (Fig. 6C), was also observed in bulk organic stable carbon isotope records ($\delta^{13}C_{org}$) from the York Canyon section (New Mexico), Hauso Flat (Montana), and at the Raton Basin, Hell Creek Road, and Pyramid Butte sections (North Dakota), in the Western Interior of the USA (Arens and Jahren, 2000; Beerling et al., 2001; Schimmelmann and DeNiro, 1984). Moreover, previous bulk inorganic stable carbon isotope records ($\delta^{13}C_{carb}$) from several worldwide K-Pg sections, such as Zumaia (Spain), Gubbio (Italy), El Kef (Tunisia), ODP site 1049 (North Atlantic), ODP site 1262 (South Atlantic) and ODP site 1209 (Pacific), (Gilabert et al., 2024 and references therein), have shown the same increased values. The evidence of a similar shift in $\delta^{13}C_{HMW}$ and by inference in higher vascular plants – suggests a shift in $\delta^{13}C$ in atmospheric CO_2 prior to the K-Pg boundary, although the aforementioned environmental controls, e.g. decreased humidity or lower pCO_2, cannot be precluded.

Similarly, the decrease, ~2‰ negative shift, in $\delta^{13}C_{HMW}$ at the ejecta layer (unit b) is consistent with previous $\delta^{13}C_{HMW}$ records observed by Arinobu et al. (1999) in C_{29} *n*-alkanes at the same Caravaca site, suggesting an injection of ^{13}C-depleted OM into the atmosphere (Birch et al., 2016). The putative input of CO_2 from breakdown of the carbonate-rich target rock of the Chicxulub impact would release isotopically heavy CO_2 into the atmosphere (Gardner and Gilmour, 2002; O'Keefe and Ahrens, 1989), and as such a positive excursion would be expected in $\delta^{13}C_{HMW}$. The lack of a $\delta^{13}C$ positive excursion in higher terrestrial plant derived biomarkers in the Caravaca section supports calculations by (Arinobu et al., 1999), who suggested that a negative carbon isotope excursion (from 1.4‰ – 2.8‰) could reflect a geologically instantaneous burning of ca. 18–24% of terrestrial aboveground biomass, although there is still debate about how extensive wildfires were after the boundary (e.g. Morgan et al., 2022). In addition, the hydrocarbons present in the target rock could have also contributed to the negative atmospheric CIE (Lyons et al., 2020; Kaiho et al., 2016). Lyons et al. calculated that 7.5×10^{14} to 2.5×10^{15} g of black carbon was released from the target rock by the Chicxulub impact. An increase in CO_2 could also lead to an increase in ε_p and an associated decrease in $\delta^{13}C_{HMW}$ values (Arens and Jahren, 2000; Cui and Schubert, 2016), amplifying the impact of a shift in the carbon isotopic composition of the atmosphere. Other works, however, interpret changes in atmospheric $\delta^{13}C$ CO_2 as a response to various climatic and eustatic factors (Gröcke et al., 1999; Kaiho et al., 1996). Regardless of mechanism, our $\delta^{13}C$ profile reveals the value of longer-term records that contextualise the variation occurring immediately following the impact. In this case, it appears that the impact caused a dramatic but transient impact on the carbon cycle and this occurred against a background of changing climatic conditions.

5.2. *Changes in organic matter source*

Consistent with environmental change occurring not just at the K-Pg boundary but preceding and following it, biomarkers ratios (and especially those related to marine vs terrestrial OM inputs, Fig. 8) are rather variable through the Caravaca K-Pg section, and major changes occur in the MARs (Fig. 9). Intriguingly, although the MARs of many biomarkers

decrease across the K-Pg boundary, marine (or aquatic) OM inputs appear to have increased prior to the K-Pg boundary and persisted across it (ejecta and boundary clay layer).

The uppermost Cretaceous sediments (unit a), from 22 kyr to 5 kyr before the K-Pg mass extinction, are dominated by a typical terrestrial OM assemblage, reflected by high HMW/total *n*-alkane ratios, high TARs (Fig. 8) and low pristane and phytane relative MARs (Fig. 9B). However, the CPIs and MARs of HMW *n*-alkanes are low and close to 1 (Fig. 8), suggesting that these inputs are at least partially from either highly altered terrestrial inputs or reworked ancient OM. Moreover, MARs of other biomarkers, including LMW *n*-alkanes, steranes and hopanes are still high. All of these are consistent with a significant and diverse variety of marine and terrestrial OM inputs.

In the final ~5 kyr of the Cretaceous (~20 cm before K-Pg mass extinction event), organic inputs begin to change, and this could reflect a late Cretaceous change in environment regime related to higher temperature and higher marine productivity (Gilabert et al., 2024) or as well as result of the Deccan Trap eruption (e.g., O'Connor et al., 2024). Pristane and phytane concentrations increase, albeit with high variability, and LMW/total *n*-alkane ratios increase (while TARs decrease). These persist through the ejecta layer (unit b) and boundary layer (unit c) and into the lower part of unit d. These changes in biomarker assemblage suggest transiently increased marine inputs. At the same time, CPIs dramatically increase and reach maximum values in the boundary layer, suggesting a pulse of relatively fresh and less reworked higher plant inputs, which could have been associated with increased nutrient inputs. Changes in the C_{27}/C_{29} sterane ratios could reflect a change in algal community (i.e. Schwark and Empt, 2006) associated with a productivity increase. However, the sterane to hopane ratio [S/(S + H)] decreases, suggesting decreased (eukaryotic) phytoplankton inputs relative to bacterial ones (e.g., Love and Zumberge, 2021) – although that could be explained by increased cyanobacterial abundances. Therefore, we suggest that the uppermost Cretaceous and lowermost Paleogene were associated with increased inputs from relatively fresh marine OM, as well as reworked marine OM (supporting by the abundant reworked Cretaceous planktonic foraminifer specimens observed in our biostratigraphic analysis, see Section 4.1 and Fig. 3) and relatively fresh terrestrial OM. This was accompanied by changes in the algal assemblage, driving changes in sterane distributions and sterane to hopane ratios. Intriguingly, these changes all begin at the same time as the long-term increase in $\delta^{13}C_{HMW}$, but they do not appear to respond to the dramatic post-K-Pg -CIE. This suggests that the biomarker assemblages were driven primarily by local climatic and environmental changes unrelated to the impact that caused a pulse in marine productivity from 5 kyrs before to 30 kyrs after the K-Pg mass extinction event.

Within the boundary clay layer (unit c), which represents the first 10 kyr post-K-Pg, biomarker assemblages are initially like those of the ejecta layer. LMW/total *n*-alkane ratios reached maximum values (Fig. 8A). The C_{27}/C_{29} sterane ratio, C_{27} sterane concentration (%) and pristane + phytane MARs are similar to those from the latest Cretaceous (Figs. 8A-B and 9) and HMW/total *n*-alkane and TAR ratios are lower (Fig. 8B). Therefore, it appears that these local environmental and ecological changes associated with the latest Cretaceous and the K-Pg boundary persisted for about 10 kyr.

5.3. The post-K-Pg phytoplankton community

The Chicxulub impact caused a global decrease in productivity in the world's oceans (Alvarez et al., 1980; Schulte et al., 2010; Smit and Hertogen, 1980). This has been evident in some biomarker assemblages from proximal sites (e.g., Trim Cane Creek and Starkville sections, USA), where a decrease in the flux of marine OM to the seafloor in the immediate aftermath of the impact and mass extinction persisted through the first ~160 kyr after the K-Pg event (Sosa-Montes de Oca et al., 2024). But it seems not to be the same for distal sites (e.g., Demark, Spain and New Zealand; (Sepúlveda et al., 2009; Sosa-Montes de Oca et al., 2023, Sosa-Montes de Oca et al., 2021). These distal places, although with some local differences, likely reflect a soft impact in biomarkers communities and minimum changes in biomarker assemblages.

In the Caravaca section, after only 10 kyr post-impact, in the upper part of the Paleogene sediments (unit d), biomarker ratios return to those values observed at the base of the section – although biomarker MARs remain low. Low biomarker MARs, arise only partially from lower biomarker concentrations and are instead driven by lower sedimentation rates, i.e. lower carbonate MARs, than in the Cretaceous. It appears, therefore, that export productivity of calcareous primary producers (carbonate MARs) never recovered to late Cretaceous values during the entirety of our study time interval, including the first 220 kyr after K-Pg mass extinction. This is in the previously suggested 1.8 Myr timeframe for global recovery of the biological pump, as defined by stable carbon isotopic values (Birch et al., 2016). However, the response of the wider community, as reflected by biomarker MARs, is more complex, documenting both a similar dramatic decrease and slow recovery of some algae (steranes), bacteria (hopanes) and higher plants (HMW *n*-alkanes) (Fig. 9A, C-D), although with a pulse of productivity (pristane and phytane; LMW *n*-alkanes, see Fig. 9A-B) preceding and spanning, from 5 kyrs before to 30 kyrs after, the K-Pg boundary. Moreover, all algal and bacterial biomarkers persist though the section (with the exception of the ejecta layer itself).

This response differs to biomarker records derived from a recently studied proximal K-Pg section in the Gulf Coast Plain (Sosa-Montes de Oca et al., 2024), where pristane and phytane MARs decreased dramatically at the K-Pg, suggesting a transient collapse in primary productivity. There is spatial heterogeneity in productivity in the post-impact oceans worldwide (e.g., Birch et al., 2021; Esmeray-Senlet et al., 2015; Hull and Norris, 2011; Morgan et al., 2022), and different biomarker responses likely reflect the role of local factors in mediating the global effect of the impact; for example, the Gulf Coast Plain section is a middle/inner shelf proximal site and the Caravaca section is a bathyal distal site, representing two different ecosystems. Moreover, we note that the increase in productivity in the Caravaca section began prior to the impact, suggesting that at this distal site, local environmental change exerted a more direct influence on algal production than the impact. Climate and environmental changes preceding the K-Pg meteorite impact have been well documented (Gilabert et al., 2024), and local responses will reflect the interaction of these with all of those associated with the impact (Kring, 2007; Lyons et al., 2020; Morgan et al., 2022).

6. Conclusions

We analysed lipid biomarkers, inorganic geochemical ratios and stable isotopic carbon compositions in a continuous 300-cm (~242 kyrs) interval from the Caravaca K-Pg boundary section in southeast Spain, a site that is distal to the Chicxulub impact site. We used these to explore changes in sources of OM prior to and through the K-Pg. In particular, we determined the response and recovery of non-fossilizing algal (and bacterial) primary producers, as documented by biomarkers (*n*-alkanes, acyclic isoprenoids, steranes and hopanes), across an extended interval that spans ~22 kyr before to ~220 kyr after the K-Pg impact event. We observed that despite the dramatic climate and environmental changes that happened previous to and during the K-Pg impact event, all algal and bacterial biomarkers persist through the section, consistent with investigations of other distal sites. However, there are changes in the sources of OM. While higher plant (HMW *n*-alkanes) markers are highly variable in the section, some aquatic, presumably algal, biomarkers (pristane and phytane; LMW *n*-alkanes) increase preceding and spanning across the K-Pg boundary from 5 kyrs before to 30 kyrs after, perhaps reflecting a pulse of productivity. However, other presumably aquatic biomarkers exhibit more complex signals (steranes and hopanes). Collectively, this reveals a complex ecological response to climatic and environmental events in the latest Cretaceous and across the K-Pg

boundary and argues against an extended global shutdown of primary productivity.

CRediT authorship contribution statement

Claudia Sosa-Montes de Oca: Writing – review & editing, Writing – original draft, Visualization, Resources, Project administration, Methodology, Investigation, Funding acquisition, Formal analysis, Data curation, Conceptualization. **Marta Rodrigo-Gámiz:** Writing – review & editing, Validation, Supervision, Conceptualization. **Gines A. de Gea:** Writing – review & editing, Investigation, Formal analysis, Data curation. **Cristina Sequero:** Writing – review & editing, Formal analysis, Data curation. **Yiming Zhang:** Formal analysis, Data curation. **Panteleimon Prokopiou:** Formal analysis, Data curation. **José Manuel Castro:** Writing – review & editing, Formal analysis, Data curation. **Mª. Luisa Quijano:** Writing – review & editing, Data curation. **Richard D. Pancost:** Writing – review & editing, Validation, Supervision, Methodology, Investigation, Formal analysis, Data curation, Conceptualization.

Declaration of competing interest

We wish to confirm that there are no known conflicts of interest associated with this publication and there has been no significant financial support for this work that could have influenced its outcome.

We confirm that the manuscript has been read and approved by all named authors and that there are no other persons who satisfied the criteria for authorship but are not listed. We further confirm that the order of authors listed in the manuscript has been approved by all of us.

We confirm that we have given due consideration to the protection of intellectual property associated with this work and that there are no impediments to publication, including the timing of publication, with respect to intellectual property. In so doing we confirm that we have followed the regulations of our institutions concerning intellectual property.

We understand that the Corresponding Author is the sole contact for the Editorial process (including Editorial Manager and direct communications with the office). She is responsible for communicating with the other authors about progress, submissions of revisions and final approval of proofs. We confirm that we have provided a current, correct email address which is accessible by the Corresponding Author and which has been configured to accept email from (claudia.sosamontesdeoca@bristol.ac.uk).

Acknowledgments

The authors wish to thank the NERC (contract no. NE/V003917/1) and funding from the European Research Council under the European Union's Seventh Framework Programme (FP/2007-2013) and Grant Agreement number 340923 for funding GC–MS capabilities. C.S.M.O. acknowledges the Newton International post-doctoral fellowship from Royal Society (project reference NIF\R1\191430) and the two MSCA fellowships from the European Commission (projects references: 101022128-EPROAMA and 101150036-GAMES). R.D.P. acknowledges funding from UKRI for the Frontiers Research Grant "Climate, Carbon and Energy in ancient Earth Systems" (CERES). M.R.G. acknowledges post-doctoral fellowship Juan de la Cierva-Incorporación program (fellowship no. IJCI-2017-33755) and Research Group RNM-190 of the Plan Andaluz de Investigación, Desarrollo e Innovación (Junta de Andalucía). J.M.C., M.L.Q., G.A.G. and C.S. acknowledge funding from the Ministerio de Ciencia e Innovación of Spain, Project PID2023-151264NB-I00, and Research Group RNM-200 of the Plan Andaluz de Investigación, Desarrollo e Innovación (Junta de Andalucía). We also thanks to the Dirección General de Patrimonio Cultural de la Comunidad Autónoma de la Región de Murcia and, as well as to the Concejalía de Cultura del Ayuntamiento de Caravaca de la Cruz for facilitating access to do this research (EXC/164/2021) at the Barranco del Gredero K-Pg boundary outcrop.

Appendix A. Supplementary data

Supplementary data to this article can be found online at https://doi.org/10.1016/j.gloplacha.2026.105366.

Data availability

The authors confirm that all data necessary for supporting the scientific findings of this paper have been provided.

References

Aller, R.C., 1998. Mobile deltaic and continental shelf muds as suboxic, fluidized bed reactors. Mar. Chem. 61, 143–155.
Alvarez, L.W., Alvarez, W., Asaro, F., Michel, H.V., 1980. Extraterrestrial cause for the Cretaceous-Tertiary extinction. Science (1979) 208, 1095–1108.
Alvarez, S.A., Gibbs, S.J., Bown, P.R., Kim, H., Sheward, R.M., Ridgwell, A., 2019. Diversity decoupled from ecosystem function and resilience during mass extinction recovery. Nature 574, 242–245. https://doi.org/10.1038/s41586-019-1590-8.
Arenillas, I., Arz, J.A., 2000. Parvularugoglobigerina eugubina type-sample at ceselli (Italy) planktic foraminiferal assemblage and lowermost danian biostratigraphic implications. Riv. Ital. Paleontol. Stratigr. 106, 379–390.
Arenillas, I., Arz, J.A., 2013. Origin and evolution of the planktic foraminiferal family eoglobigerinidae blow during the early Danian (Paleocene). Revista Mexicana de Ciencias Geologicas 30, 159–177.
Arenillas, I., Arz, J., Molina, E., 2004. A new high-resolution planktic foraminiferal zonation and subzonation for the lower Danian. Lethaia 37, 79–95. https://doi.org/10.1080/00241160310005097.
Arenillas, I., Arz, J.A., Náñez, C., 2007. Morfología, Biometría y Taxonomía de foraminíferos planctónicos del Daniense basal: Palaeoglobigerina n. gen. Revista Española de Paleontología 22 (1), 21–62.
Arens, N.C., Jahren, A.H., 2000. Carbon isotope excursion in atmospheric CO 2 at the Cretaceous-Tertiary boundary: evidence from terrestrial sediments. Palaios 15, 314. https://doi.org/10.2307/3515539.
Arinobu, T., Ishiwatari, R., Kaiho, K., Lamolda, M.A., 1999. Spike of pyrosynthetic polycyclic aromatic hydrocarbons associated with an abrupt decrease in δ13C of a terrestrial biomarker at the Cretaceous-Tertiary boundary at Caravaca, Spain. Geology 27, 723–726. https://doi.org/10.1130/0091-7613(1999)027<0723.
Arinobu, T., Ishiwatari, R., Kaiho, K., Lamolda, M.A., Seno, H., 2005. Abrupt and massive influx of terrestrial biomarkers into the marine environment at the Cretaceous-Tertiary boundary, Caravaca, Spain. Palaeogeogr. Palaeoclimatol. Palaeoecol. 224, 108–116. https://doi.org/10.1016/j.palaeo.2005.03.032.
Artemieva, N., Morgan, J., 2009. Modeling the formation of the K-Pg boundary layer. Icarus 201, 768–780. https://doi.org/10.1016/j.icarus.2009.01.021.
Artemieva, N., Morgan, J., 2020. Global K-Pg layer deposited from a dust cloud. Geophys. Res. Lett. 47, 1–8. https://doi.org/10.1029/2019GL086562.
Arz, J.A., Molina, E., 2002. Bioestratigrafía y cronoestratigrafía con foraminíferos planctónicos del Campaniense superior y Maastrichtiense de latitudes subtropicales y templadas (España, Francia y Tunicia). Neues Jahrb. Geol. Palaontol. Abh. 224, 161–195.
Arz, J.A., Arenillas, I., Molina, E., Sepúlveda, R., 2000. Planktonic foraminiferal stability inthe Upper Maastrichtian and the catastrophic mass extionction at the Cretaceous-Tertiary (K/T) boundary at Caravaca (Spain) | La estabilidad evolotiva de los foraminíferos planctónicos en el Maastrichtiense superior y. Rev. Geol. Chile 27, 27–44.
Arz, J.A., Arenillas, I., Náñez, C., 2010. Morphostatistical analysis of Maastrichtian populations of Guembelitria from El Kef, Tunisia. J. Foraminifer. Res. 40 (2), 148–164. https://doi.org/10.2113/gsjfr.40.2.148.
Beerling, D.J., Lomax Jr., B.H., Nichols, D.J., Pillmore, C.L., Handley, L.L., Scrimgeour, C.M., 2001. Evidence for the recovery of terrestrial ecosystems ahead of marine primary production following a biotic crisis at the Cretaceous–Tertiary boundary. J. Geol. Soc. Lond. 158, 737–740.
Berggren, W.A., Pearson, P.N., 2005. A revised tropical to subtropical Paleocene planktonic foraminiferal zonation. J. Foraminifer. Res. 35, 279–298. https://doi.org/10.2113/35.4.279.
Birch, H.S., Coxall, H.K., Pearson, P.N., Kroon, D., Schmidt, D.N., 2016. Partial collapse of the marine carbon pump after the Cretaceous-Paleogene boundary. Geology 44, 287–290. https://doi.org/10.1130/G37581.1.
Birch, H., Schmidt, D.N., Coxall, H.K., Kroon, D., Ridgwell, A., 2021. Ecosystem function after the K/Pg extinction: decoupling of marine carbon pump and diversity. Proc. R. Soc. B Biol. Sci. 288. https://doi.org/10.1098/rspb.2021.0863.
Bourbonniere, R.A., Meyers, P.A., 1996. Sedimentary geolipid records of historical changes in the watersheds and productivities of Lakes Ontario and Erie. Limnol. Oceanogr. 41, 352–359. https://doi.org/10.4319/lo.1996.41.2.0352.
Bralower, T.J., Cosmidis, J., Heaney, P.J., Kump, L.R., Morgan, J.V., Harper, D.T., Lyons, S.L., Freeman, K.H., Grice, K., Wendler, J.E., Zachos, J.C., Artemieva, N., Chen, S.A., Gulick, S.P.S., House, C.H., Jones, H.L., Lowery, C.M., Nims, C., Schaefer, B., Thomas, E., Vajda, V., 2020. Origin of a global carbonate layer deposited in the aftermath of the Cretaceous-Paleogene boundary impact. Earth Planet. Sci. Lett. 548, 116476. https://doi.org/10.1016/j.epsl.2020.116476.

Bray, E.E., Evans, E.D., 1961. Distribution of n-paraffins as a clue to recognition of source beds. Geochim. Cosmochim. Acta 22, 2–15. https://doi.org/10.1016/0016-7037(61)90069-2.

Calvert, S.E., Pedersen, T.F., 1993. Geochemistry of recent oxic and anoxic marine sediments: Implications for the geological record. Mar. Geol. 113, 67–88.

Carmichael, S.K., Waters, J.A., Königshof, P., Suttner, T.J., Kido, E., 2019. Paleogeography and paleoenvironments of the late Devonian Kellwasser event: a review of its sedimentological and geochemical expression. Glob. Planet. Chang. 183, 102984. https://doi.org/10.1016/j.gloplacha.2019.102984.

Caron, M., 1985. Cretaceous planktic foraminifera. In: Bolli, H.M., Saunders, J.B., Perch-Nielsen, K. (Eds.), Plankton Stratigraphy. Cambridge University Press, Cambridge, p. 17e86.

Cranwell, P.A., Eglinton, G., Robinson, N., 1987. Lipids of aquatic organisms as potential contributors to lacustrine sediments-II. Org. Geochem. 11, 513–527. https://doi.org/10.1016/0146-6380(87)90007-6.

Cui, Y., Schubert, B.A., 2016. Quantifying uncertainty of past pCO2 determined from changes in C3 plant carbon isotope fractionation. Geochim. Cosmochim. Acta 172, 127–138. https://doi.org/10.1016/j.gca.2015.09.032.

De Lange, G.J., Van der Sloot, H.A., Wijkstra, J., 1987. Implications of the diagenetic mobility of Ir for the interpretation of the anomaly at the K/T boundary. Geol. Soc. Spec. Publ. 31, 147–165.

Dean, R.A., Whitehead, E.V., 1961. The occurrence of Phytane in petroleum. Tetrahedron Lett. 21, 768–770.

D'Hondt, S., 2005. Consequences of the cretaceous/paleogene mass extinction for marine ecosystems. Annu. Rev. Ecol. Evol. Syst. 36, 295–317. https://doi.org/10.1146/annurev.ecolsys.35.021103.105715.

Diefendorf, A.F., Mueller, K.E., Wing, S.L., Koch, P.L., Freeman, K.H., 2010. Global patterns in leaf 13C discrimination and implications for studies of past and future climate. Proc. Natl. Acad. Sci. USA 107, 5738–5743. https://doi.org/10.1073/pnas.0910513107.

Diefendorf, A.F., Freeman, K.H., Wing, S.L., Graham, H.V., 2011. Production of n-alkyl lipids in living plants and implications for the geologic past. Geochim. Cosmochim. Acta 75, 7472–7485. https://doi.org/10.1016/j.gca.2011.09.028.

Eglinton, G., Clavin, M., 1967. Certain rocks as much as three billion years old have been found to contain organic compounds. What these compounds are and how they may have originated in living matter is under active study. Sci. Am. 216, 32–43.

Eglinton, G., Hamilton, R.J., 1967. Leaf epicuticular waxes. Science (1979) 156, 1322–1335. https://doi.org/10.1126/science.156.3780.1322.

Esmeray-Senlet, S., Wright, J.D., Olsson, R.K., Miller, K.G., Browning, J.V., Quan, T.M., 2015. The cretaceous/paleogene mass extinction. Paleoceanography 30, 718–738. https://doi.org/10.1002/2014PA002724.Received.

Farquhar, G.D., O'Leary, M.H., Berry, J.A., 1982. On the relationship between carbon isotope discrimination and the intercellular carbon dioxide concentration in leaves. Funct. Plant Biol. 9, 121–137.

Farquhar, G.D., Ehleringer, J.R., Hubick, K.T., 1989. Carbon isotope discrimination and photosynthesis. Annu. Rev. Plant Physiol. Plant Mol. Biol. 40, 503–537. https://doi.org/10.1146/annurev.pp.40.060189.002443.

Gardner, A.F., Gilmour, I., 2002. Organic geochemical investigation of terrestrial Cretaceous-Tertiary boundary successions from Brownie Butte, Montana, and the Raton Basin, New Mexico. Spec. Paper Geol. Soc. Am. 356, 351–362.

Gearing, P., Gearing, J.N., Lytle, T.F., Lytle, J.S., 1976. Hydrocarbons in 60 Northeast Gulf of Mexico shelf sediments: a preliminary survey. Geochim. Cosmochim. Acta 40, 1005–1017. https://doi.org/10.1016/0016-7037(76)90043-0.

Gilabert, V., Arenillas, I., Arz, J.A., Batenburg, S.J., Robinson, S.A., 2021. Multiproxy analysis of paleoenvironmental, paleoclimatic and paleoceanographic changes during the early Danian in the Caravaca section (Spain). Palaeogeogr. Palaeoclimatol. Palaeoecol. 576. https://doi.org/10.1016/j.palaeo.2021.110513.

Gilabert, V., Batenburg, S.J., Arz, J.A., Baumann, N.B., Regelous, M., Arenillas, I., 2024. Evaluation of the main drivers of environmental and climatic changes of the sea-surface across the Cretaceous-Paleogene transition: a global perspective. Geobios 88–89, 125–137. https://doi.org/10.1016/j.geobios.2024.08.011.

Glass, B.P., Burns, C.A., 1987. Late eocene crystal-bearing spherules - 2 layers or one - a reply. Meteoritics 23, 265–279.

Goderis, S., Tagle, R., Belza, J., Smit, J., Montanari, A., Vanhaecke, F., Erzinger, J., Claeys, P., 2013. Reevaluation of siderophile element abundances and ratios across the Cretaceous-Paleogene (K-Pg) boundary: Implications for the nature of the projectile. Geochim. Cosmochim. Acta 120, 417–446. https://doi.org/10.1016/j.gca.2013.06.010.

Gradstein, F., Ogg, J., Schmitz, M., Ogg, G., 2020. Geological Time Scale 2020. Elsevier Science, pp. 21–32. https://doi.org/10.1016/B978-0-12-824360-2.00002-4.

Gröcke, D.R., Hesselbo, S.P., Jenkyns, H.C., 1999. Carbon-isotope composition of lower cretaceous fossil wood: ocean-atmosphere chemistry and relation to sea-level change. Geology 27, 155–158. https://doi.org/10.1130/0091-7613(1999)027<0155:CICOLC>2.3.CO;2.

Henehan, M.J., Ridgwell, A., Thomas, E., Zhang, S., Alegret, L., Schmidt, D.N., Rae, J.W. B., Witts, J.D., Landman, N.H., Greene, S.E., Huber, B.T., Super, J.R., Planavsky, N. J., Hull, P.M., 2019. Rapid Ocean acidification and protracted Earth system recovery followed the end-cretaceous Chicxulub impact. Proc. Natl. Acad. Sci. USA 116, 22500–22504. https://doi.org/10.1073/pnas.1905989116.

Hildebrand, A.R., Penfield, G.T., Kring, D.A., Pilkington, M., Jacobsen, S.B., Boynton, W. V., 1991. Chicxulub Crater: a possible cretaceous/Tertiary boundary impact crater on the Yucatán Peninsula, Mexico. Geology 19, 867. https://doi.org/10.1130/0091-7613(1991)019<0867:CCAPCT>2.3.CO;2.

Huang, W.Y., Meinschew, W..G., 1979. Sterols as ecological indicators. Geochim. Cosmochim. Acta 43, 739–745.

Hull, P.M., Norris, R.D., 2011. Diverse patterns of ocean export productivity change across the Cretaceous-Paleogene boundary: new insights from biogenic barium. Paleoceanography 26, PA3205. https://doi.org/10.1029/2010PA002082.

Hull, P.M., Bornemann, A., Penman, D.E., Henehan, M.J., Norris, R.D., Wilson, P.A., Blum, P., Alegret, L., Batenburg, S.J., Bown, P.R., Bralower, T.J., Cournede, C., Deutsch, A., Donner, B., Friedrich, O., Jehle, S., Kim, H., Kroon, D., Lippert, P.C., Loroch, D., Moebius, I., Moriya, K., Peppe, D.J., Ravizza, G.E., Röhl, U., Schueth, J. D., Sepúlveda, J., Sexton, P.F., Sibert, E.C., Summons, R.E., Thomas, E., Westerhold, T., Whiteside, J.H., Yamaguchi, T., Zachos, J.C., 2020. On impact and volcanism across the Cretaceous-Paleogene boundary. Science 1979 (367), 266–272.

Husson, D., Galbrun, B., Gardin, S., Thibault, N., 2014. Tempo and duration of short-term environmental perturbations across the Cretaceous-Paleogene boundary. Stratigraphy 11, 159–171. https://hal.archives-ouvertes.fr/hal-01092775.

Kaiho, K., Lamolda, M.A., 1999. Catastrophic extinction of planktonic foraminifera at the Cretaceous-Tertiary boundary evidenced by stable isotopes and foraminiferal abundance at Caravaca, Spain. Geology 27, 355–358.

Kaiho, K., Arinobu, T., Ishiwatari, R., Morgans, H.E.G., Okada, H., Takeda, N., Tazaki, K., Zhou, G., Kajiwara, Y., Matsumoto, R., Hirai, A., Niitsuma, N., Wada, H., 1996. Lasted Paleocene benthic foraminiferal extinction and environmental changes at Tawanui , New Zealand. Paleoceanography 11, 447–465.

Kaiho, K., Oshima, N., Adachi, K., Adachi, Y., Mizukami, T., Fujibayashi, M., Saito, R., 2016. Global climate change driven by soot at the K-Pg boundary as the cause of the mass extinction. Sci. Rep. 6, 28427. https://doi.org/10.1038/srep28427.

Kohn, M.J., 2010. Carbon isotope compositions of terrestrial C3 plants as indicators of (paleo)ecology and (paleo)climate. Proc. Natl. Acad. Sci. USA 107, 19691–19695. https://doi.org/10.1073/pnas.1004933107.

Kring, D.A., 2007. The Chicxulub impact event and its environmental consequences at the Cretaceous-Tertiary boundary. Palaeogeogr. Palaeoclimatol. Palaeoecol. 255, 4–21. https://doi.org/10.1016/j.palaeo.2007.02.037.

Kvenvolden, K.A., 1967. Normal fatty acids in sediments. J. Am. Oil Chem. Soc. 44, 628–636. https://doi.org/10.1007/BF02680031.

Kyte, F.T., 1998. A meteorite from the cretaceous/tertiary boundary. Nature 396, 237–239.

Laska, W., Rodríguez-Tovar, F.J., Uchman, A., 2017. Evaluating macrobenthic response to the Cretaceous–Palaeogene event: a high-resolution ichnological approach at the Agost section (SE Spain). Cretac. Res. 70, 96–110. https://doi.org/10.1016/j.cretres.2016.10.003.

Li, S., Grasby, S.E., Zhao, X., Chen, J., Zheng, D., Wang, H., Fang, Y., Zhang, Q., Yu, T., Tian, J., Du, S., Jarzembowski, E.A., Wang, Q., Zhang, H., Wan, X., Wang, B., 2022. Mercury evidence of Deccan volcanism driving the latest Maastrichtian warming event. Geology 50 (10), 1140–1144.

Loeblich Jr., A.R., Tappan, H., 1987. Foraminiferal Genera and their Classification, 2. Van Nostrand Reinhold Company, New York, p. 970.

Love, G.D., Zumberge, J.A., 2021. Emerging Patterns in Proterozoic Lipid Biomarker Records, Emerging Patterns in Proterozoic Lipid Biomarker Records. Cambridge University Press. https://doi.org/10.1017/9781108847117.

Lowery, C.M., Bralower, T.J., 2022. Elevated post K-Pg export productivity in the Gulf of Mexico and Caribbean. Paleoceanogr. Paleoclimatol. 37. https://doi.org/10.1029/2021PA004400.

Lowery, C.M., Bown, P.R., Fraass, A.J., Hull, P.M., 2020. Ecological response of plankton to environmental change: thresholds for extinction Christopher. Annu. Rev. Earth Planet. Sci. 48, 16.1–16.27. https://doi.org/10.1146/annurev-earth-081619-052818.

Luterbacher, H.P., Premoli Silva, I., 1964. Biostratigrafia del límite Cretaceo–Terziario nell' Appennino Centrale. Riv. Ital. Paleontol. Stratigr. 70, 67–128.

Lyons, S.L., Karp, A.T., Bralower, T.J., Grice, K., Schaefer, B., Gulick, S.P.S., Morgan, J. V., Freeman, K.H., 2020. Organic matter from the Chicxulub crater exacerbated the K-Pg impact winter. Proc. Natl. Acad. Sci. USA 117, 25327–25334. https://doi.org/10.1073/pnas.2004596117.

Mackenzie, A.S., Patience, R.L., Maxwell, J.R., Vandenbroucke, M., Durand, B., 1980. Molecular parameters of maturation in the Toarcian shales, Paris Basin, France—I. Changes in the configurations of acyclic isoprenoid alkanes, steranes and triterpanes. Geochim. Cosmochim. Acta 44, 1709–1721. https://doi.org/10.1016/0016-7037(80)90222-7.

Martínez-Ruiz, F., Ortega-Huertas, M., Palomo, I., Acquafredda, P., 1997. Quench textures in altered spherules from the Cretaceous-Tertiary boundary layer at Agost and Caravaca, SE Spain. Sediment. Geol. 113, 137–147. https://doi.org/10.1016/S0037-0738(97)00057-2.

Metsana-Oussaid, F., Belhai, D., Arenillas, I., Arz, J.A., Gilabert, V., 2019. New sections of the Cretaceous–Paleogene transition in the southwestern Tethys (Médéa, northern Algeria): planktic foraminiferal biostratigraphy and biochronology. Arab. J. Geosci. https://doi.org/10.1007/s12517-019-4402-4.

Mizukami, T., Kaiho, K., Oba, M., 2013. Significant changes in land vegetation and oceanic redox across the cretaceous/paleogene boundary. Palaeogeogr. Palaeoclimatol. Palaeoecol. 369, 41–47. https://doi.org/10.1016/j.palaeo.2012.09.020.

Molina, E., Alegret, L., Arenillas, I., Arz, J.A., 2005. The cretaceous/Paleogene boundary at the Agost section revisited : paleoenvironmental reconstruction and mass extinction pattern. J. Iber. Geol. 31, 135–148.

Morford, J.L., Emerson, S., 1999. The geochemistry of redox sensitive trace metals in sediments. Geochim. Cosmochim. Acta 63, 1735–1750. https://doi.org/10.1016/S0016-7037(99)00126-X.

Morgan, J.V., Bralower, T.J., Brugger, J., Wünnemann, K., 2022. The Chicxulub impact and its environmental consequences. Nat. Rev. Earth Environ. https://doi.org/10.1038/s43017-022-00283-y.

Nederbract, A.J., 1991. Late cretaceous biostratigraphy and development of Heterohelicidae (planktonic foraminifera). Micropaleontology 37 (4), 329–372.
O'Connor, L.K., Jerrett, R.M., Price, G.D., Lyson, T.R., Lengger, S.K., Peterse, F., Bart, E., van Dongen, B.E., 2024. Terrestrial evidence for volcanogenic sulfate-driven cooling event ~30 kyr before the Cretaceous–Paleogene mass extinction. Sci. Adv. 10, eado5478. https://doi.org/10.1126/sciadv.ado5478.
O'Keefe, J.D., Ahrens, T.J., 1989. Impact production of CO_2 by the cretaceous/Tertiary extinction bolide and the resultant heating of the Earth. Nature 338, 247–249. https://doi.org/10.1038/338247a0.
Olsson, R.K., Hemleben, C., Berggren, W.A., Huber, B.T., 1999. Atlas of paleocene planktonic foraminifera. Smithson. Contrib. Paleobiol. 85, 1–252. https://doi.org/10.5479/si.00810266.85.1.
Ourisson, G., Albrecht, P., Rohmer, M., 1979. The Hopanoids: palaeochemistry and biochemistry of a group of natural products. Pure Appl. Chem. 51, 709–729. https://doi.org/10.1351/pac197951040709.
Pälike, H., 2013. Impact and extinction. Science (1979) 339, 655–656.
Pendoley, K., 1992. Hydrocarbons in Rowley Shelf (Western Australia) oysters and sediments. Mar. Pollut. Bull. 24, 210–215. https://doi.org/10.1016/0025-326X(92)90532-B.
Peters, K.E., Moldowan, J.M., 1991. Effects of source, thermal maturity, and biodegradation on the distribution and isomerization of homohopanes in petroleum. Org. Geochem. 17, 47–61. https://doi.org/10.1016/0146-6380(91)90039-M.
Peters, K.E., Peters, K.E., Walters, C.C., Moldowan, J.M., 2005. The Biomarker Guide. Cambridge University Press.
Popp, B.N., Takigiku, R., Hayes, J.M., Louda, J.W., Baker, E.W., 1989. The post-Paleozoic chronology and mechanism of 13C depletion in primary marine organic matter. Am. J. Sci. 289, 436–454. https://doi.org/10.2475/ajs.289.4.436.
Rieley, G., Collier, R.J., Jones, D.M., Eglinton, G., Eakint, P.A., Fallickt, A.E., 1991. Sources of sedimentary lipids deduced from stable carbon- isotope analyses of individual compounds. Nature 352, 425–427.
Robaszynski, F., Caron, M., Gonzales, J.M., Wonders, A.H. (Eds.), 1984. Rev. Micropaleontol. 26, 145–305.
Rodríguez-Tovar, F.J., 2005. Fe-oxide spherules infilling Thalassinoides burrows at the Cretaceous-Paleogene (K-P) boundary: evidence of a near-contemporaneous macrobenthic colonization during the K-P event. Geology 33, 585–588. https://doi.org/10.1130/G21527.1.
Rodríguez-Tovar, F.J., 2024. Evaluating tracemarker recovery after the Cretaceous-Paleogene (K-Pg) boundary event: different biotic responses at the Caravaca section. J. Iber. Geol. 50, 487–501. https://doi.org/10.1007/s41513-024-00235.
Rodríguez-Tovar, F.J., Uchman, A., 2004. Ichnotaxonomic analysis of the cretaceous/palaeogene boundary interval in the Agost section, South-East Spain. Cretac. Res. 25, 635–647. https://doi.org/10.1016/j.cretres.2004.06.003.
Rodríguez-Tovar, F.J., Uchman, A., 2006. Ichnological analysis of the Cretaceous-Palaeogene boundary interval at the Caravaca section, SE Spain. Palaeogeogr. Palaeoclimatol. Palaeoecol. 242, 313–325. https://doi.org/10.1016/j.palaeo.2006.06.006.
Rodríguez-Tovar, F.J., Martínez-Ruiz, F., Bernasconi, S.M., 2006. Use of high-resolution ichnological and stable isotope data for assessing completeness of a K-P boundary section, Agost, Spain. Palaeogeogr. Palaeoclimatol. Palaeoecol. 237, 137–146. https://doi.org/10.1016/j.palaeo.2005.11.019.
Rontani, J.F., Volkman, J.K., 2003. Phytol degradation products as biogeochemical tracers in aquatic environments. Org. Geochem. 34, 1–35.
Schaefer, B., Grice, K., Coolen, M.J.L., Summons, R.E., Cui, X.X., Bauersachs, T., Schwark, L., Böttcher, M.E., Bralower, T.J., Lyons, S.L., Freeman, K.H., Cockell, C.S., Gulick, S.S., Morgan, J.V., Whalen, M.T., Lowery, C.M., Vajda, V., 2020. Microbial life in the nascent chicxulub crater. Geology 48, 1–5. https://doi.org/10.3997/2214-4609.201902850.
Schimmelmann, A., DeNiro, M.J., 1984. Elemental and stable isotope variations of organic matter from a terrestrial sequence containing the cretaceous/Tertiary boundary at York Canyon, New Mexico. Earth Planet. Sci. Lett. 68, 392–398. https://doi.org/10.1016/0012-821X(84)90124-9.
Schneider, H., Gelpi, E., Bennett, E.O., Oró, J., 1970. Fatty acids of geochemical significance in microscopic algae. Phytochemistry 9, 613–617. https://doi.org/10.1016/S0031-9422(00)85701-5.
Schoene, B., Samperton, K.M., Eddy, M.P., Keller, G., Adatte, T., Bowring, S.A., Khadri, S. F.R., Gertsch, B., 2015. U-Pb geochronology of the Deccan Traps and relation to the end-cretaceous mass extinction. Science 1979 (347), 182–184. https://doi.org/10.1126/science.aaa0118.
Schoene, Bl, Eddy, M.P., Samperton, K.M., Keller, C.B., Keller, G., Adatte, T., Khadri, S.F. R., 2019. U-Pb constraints on pulsed eruption of the Deccan Traps across the end-cretaceous mass extinction. Science 1979 (363), 862–866. https://doi.org/10.1126/science.aau2422.
Schouten, S., Hopmans, E.C., Sinninghe Damsté, J.S., 2013. The organic geochemistry of glycerol dialkyl glycerol tetraether lipids: a review. Org. Geochem. 54, 19–61. https://doi.org/10.1016/j.orggeochem.2012.09.006.
Schulte, P., Alegret, L., Arenillas, I., Arz, J.A., Barton, P.J., Bown, P.R., Bralower, T.J., Christeson, G.L., Claeys, P., Cockell, C.S., Collins, G.S., Deutsch, A., Goldin, T.J., Goto, K., Grajales-Nishimura, J.M., Grieve, R.A.F., Gulick, S.P.S., Johnson, K.R., Kiessling, W., Koeberl, C., Kring, D.A., MacLeod, K.G., Matsui, T., Melosh, J., Montanari, A., Morgan, J.V., Neal, C.R., Nichols, D.J., Norris, R.D., Pierazzo, E., Ravizza, G., Rebolledo-Vieyra, M., Reimold, W.U., Robin, E., Salge, T., Speijer, R.P., Sweet, A.R., Urrutia-Fucugauchi, J., Vajda, V., Whalen, M.T., Willumsen, P.S., 2010. The chicxulub asteroid impact and mass extinction at the cretaceous-paleogene boundary. Science 327, 1214–1218. https://doi.org/10.1126/science.1177265.
Schwark, L., Empt, P., 2006. Sterane biomarkers as indicators of palaeozoic algal evolution and extinction events. Palaeogeogr. Palaeoclimatol. Palaeoecol. 240, 225–236. https://doi.org/10.1016/j.palaeo.2006.03.050.
Seifert, W.K., Moldowan, J.M., 1980. The effect of thermal stress on source-rock quality as measured by hopane stereochemistry. Phys. Chem. Earth 12, 229–237. https://doi.org/10.1016/0079-1946(79)90107-1.
Sepúlveda, J., Wendler, J.E., Summons, R.E., Hinrichs, K.-U., 2009. Rapid resurgence of marine productivity after the cretaceous-paleogene mass extinction. Science 1979 (326), 129–132. https://doi.org/10.1126/science.1176233.
Sepúlveda, J., Alegret, L., Thomas, E., Haddad, E., Cao, C., Summons, R.E., 2019. Stable isotope constraints on marine productivity across the cretaceous-paleogene mass extinction. Paleoceanogr. Paleoclimatol. 34, 1195–1217. https://doi.org/10.1029/2018PA003442.
Shukolyukov, A., Lugmair, G.W., 1998. All use subject to JSTOR terms and Conditions isotopic evidence for the Cretaceous-Tertiary impactor and its type. Science 1979 (282), 927–929.
Smit, J., 1999. The global stratigraphy of the Cretaceous-Tertiary boundary impact ejecta. Annu. Rev. Earth Planet. Sci. 27, 75–113.
Smit, J., Hertogen, J., 1980. An extraterrestrial event at the Cretaceous-Tertiary boundary. Nature 285, 198–200.
Smit, J., Klaver, G., 1981. Sanidine spherules at the Cretaceous-Tertiary boundary indicate a large impact event. Nature 292, 47–49.
Smith, A.G., Hurley, A.M., Briden, J.C., 1981. Phanerozoic Paleocontinental World Maps. CUP Archive.
Sosa-Montes de Oca, C., Martínez-Ruiz, F., Rodríguez-Tovar, F.J., 2013. Bottom-water conditions in a marine basin after the Cretaceous-Paleogene impact event: timing the recovery of oxygen levels and productivity. PLoS One 8, e82242. https://doi.org/10.1371/journal.pone.0082242.
Sosa-Montes de Oca, C., Rodríguez-Tovar, F.J., Martínez-Ruiz, F., 2016. Geochemical and isotopic characterization of trace fossil infillings: new insights on tracemaker activity after the K/Pg impact event. Cretac. Res. 57, 391–401. https://doi.org/10.1016/j.cretres.2015.03.003.
Sosa-Montes de Oca, C., de Lange, G.J., Martínez-Ruiz, F., Rodríguez-Tovar, F.J., 2018a. Application of laser ablation-ICP-MS to determine high-resolution elemental profiles across the cretaceous/paleogene boundary at Agost (Spain). Palaeogeogr. Palaeoclimatol. Palaeoecol. 497, 128–138. https://doi.org/10.1016/j.palaeo.2018.02.012.
Sosa-Montes de Oca, C., de Lange, G.J., Martínez-Ruiz, F., Rodríguez-Tovar, F.J., 2018b. High-resolution data from laser ablation-ICP-MS and by ICP-OES analyses at the cretaceous/paleogene boundary section at Agost (SE Spain). Data Brief 18, 1900–1906. https://doi.org/10.1016/j.dib.2018.04.118.
Sosa-Montes de Oca, C., de Lange, G.J., Martínez-Ruiz, F., Ortega-Huertas, M., Rodríguez-Tovar, F.J., 2020. Microscale trace-element distribution across the cretaceous/Palaeogene ejecta layer at the Agost section: constraining the recovery of pre-impact conditions. Chem. Geol. 533. https://doi.org/10.1016/j.chemgeo.2019.119431.
Sosa-Montes de Oca, C., Rodrigo-Gámiz, M., Martínez-Ruiz, F., Rodríguez-Tovar, F.J., Castro, J.M., Quijano, M.L., Pancost, R.D., 2021. Minor changes in biomarker assemblages in the aftermath of the Cretaceous-Paleogene mass extinction event at the Agost distal section (Spain). Palaeogeogr. Palaeoclimatol. Palaeoecol. 569, 110310. https://doi.org/10.1016/j.palaeo.2021.110310.
Sosa-Montes de Oca, C., Taylor, K.W.R., Hollis, C.J., Huang, Y., Pancost, R.D., 2023. Variation in organic matter across the Cretaceous-Paleogene boundary in New Zealand supports the "Living Ocean" model of biotic recovery. Glob. Planet. Chang. 220. https://doi.org/10.1016/j.gloplacha.2022.104025.
Sosa-Montes de Oca, C., Witts, J.D., Lowery, C.M., Kearns, L.E., Garb, M.P., Naujokaityte, J., Myers, C.E., Landman, N.H., Pancost, R.D., 2024. Intense changes in the main source of organic carbon to the Gulf Coastal Plain following the Cretaceous-Paleogene boundary. Paleoceanogr. Paleoclimatol. 39. https://doi.org/10.1029/2024PA004887.
Sprain, C.J., Renne, P.R., Clemens, W.A., Wilson, G.P., 2018. Calibration of chron C29r: new high-precision geochronologic and paleomagnetic constraints from the Hell Creek region, Montana. Bull. Geol. Soc. Am. 130, 1615–1644. https://doi.org/10.1130/B31890.1.
Swisher Ill, C.C., Grajales-Nishimura, J.M., Montanari, A., Margolis, S.V., Claeys, P., Alvarez, W., Renne, P., Cedillo-Pardo, E., Maurrasse, J.-M., Curtis, G.H., Smit, J., McWillians, M.O., 1990. Coeval 40Ar/39Ar Ages of 65.0 Million Years Ago from Chicxulub Crater Melt Rock and Cretaceous-Tertiary Boundary Tektites, P. Ortoleva, Physica.
Taylor, K.W.R., Willumsen, P.S., Hollis, C.J., Pancost, R.D., 2018. South Pacific evidence for the long-term climate impact of the cretaceous/paleogene boundary event. Earth Sci. Rev. 179, 287–302. https://doi.org/10.1016/j.earscirev.2018.02.012.
Tribovillard, N., Algeo, T.J., Lyons, T., Riboulleau, A., 2006. Trace metals as paleoredox and paleoproductivity proxies: an update. Chem. Geol. 232, 12–32. https://doi.org/10.1016/j.chemgeo.2006.02.012.
Van der Weijden, C.H., 2002. Pitfalls of normalization of marine geochemical data using a common divisor. Mar. Geol. 184, 167–187.
Wade, B.S., Pearson, P.N., Berggren, W.A., Pälike, H., 2011. Review and revision of Cenozoic tropical planktonic foraminiferal biostratigraphy and calibration to the geomagnetic polarity and astronomical time scale. Earth Sci. Rev. https://doi.org/10.1016/j.earscirev.2010.09.003.
Young, J.R., Wade, B.S., Huber, B.T., 2024. Pforams@mikrotax Website. URL. http://www.mikrotax.org/pforams.